Characterizing the role of DDX3X in DNA double strand break repair; Implications for lymphocyte biology

Michael Cargill

A dissertation submitted in partial fulfillment of the
requirements for the degree of

Doctor of Philosophy

University of Washington
2020

Reading Committee:
Edus H. Warren: Chair
Eleanor Chen
Brian Iritani
Jason Bielas
Christine Disteche

Program Authorized to Offer Degree:
Pathology

University of Washington

Abstract

Characterizing the role of DDX3X in DNA double-strand break repair; Implications for lymphocyte biology

Michael Cargill

Chair of Supervisory Committee:
Edus H. Warren
Adjunct Professor of Pathology

DDX3X is a human, ATP-dependent RNA helicase with roles throughout RNA metabolism. A number of human diseases are associated with alterations in this gene, particularly in hematological malignancies. We aimed to investigate a novel function for DDX3X in DNA double-strand break (DSB) repair and its role in lymphocyte biology. We confirmed a traditional role for DDX3X in regulating DNA DSB repair protein levels, and herein provide evidence for a novel role as an active participant in DSB repair. We propose that DDX3X is recruited to DSBs in actively transcribed regions to regulate DSB-induced RNA metabolism. Finally, we developed CRISPR/Cas9 techniques to interrogate the function of DDX3X, and its Y-homologue, in lymphocyte biology. Thus, DDX3X plays an important role in DSB repair likely consequential to lymphocyte health and disease.

Table of Contents

Acknowledgements

I would like to thank my thesis committee - Brian Iritani, Christine Disteche, Eleanor Chen, and Jason Bielas - for their long-standing support. You all have seen this body of work from its very inception and helped it grow throughout the years. This dissertation is a product of your support and I am deeply grateful.

This body of work would not be possible without the enthusiastic support of the Warren lab. Thank you for making me feel welcome and at home from day one. You are all like family to me. I am proud to have a scientific heritage full of zest, curiosity, and resiliency. To David Coffee, thank you for showing me the future of medicine. To Katie Lombardo, thank you for your grace and insight. To Chris Miller, thank you for your experience and for helping me without hesitation. To Alicia Morales, thank you for believing in me always. To Shashi Ravishankar, thank you for showing me new ways of seeing biology. To Andrea Towlerton, thank you for showing me that nothing in science is impossible. To Scott Tykodi, thank you for showing me how science can save lives. To Yuexin Xu, thank you for your boundless kindness and patience.

And to Hootie Warren, thank you for investing your time, energy, and expertise into my development as a scientist. I feel honored and have enjoyed every moment (yes, the weekends too) working with you in your lab. You have a mastery over scientific inquiry and deep passion for making the world a better place. I am a better scientist, and person, having been mentored by you.

Finally, I would like to thank my family. Your unwavering love and support has gotten me through the challenges of graduate school. Mom, Dad, and Hannah - you have been there for me every step of the way and for that, I am forever grateful.

Dedication

This is dedicated to my grandma Susie and grandma Ann.

I hope this work will, in some way, help fight human disease and suffering.

Chapter 1

Background

DDX3X Overview

Genetics

DDX3X is a gene encoding an ATP-dependent RNA helicase. Located on the p arm of the human X-chromosome in the non-pseudoautosomal region, *DDX3X* is one of the 15% of X-linked genes that escape X-inactivation and among the 19 X-linked genes paired with a Y homologue, *DDX3Y* (1, 2). The evolutionary history of these genes suggest that X-Y pairs serve house-keeping functions requiring an optimal dosage in cells thereby leading to the conservation of the Y homologues over the past 4 million years (3, 4). *DDX3X* is expressed in virtually all major tissues in humans (Ch. 3). Cross-reactive antibodies obscure the extent of DDX3X vs. DDX3Y levels in human tissues. While DDX3Y is traditionally associated with testis-specific expression, our lab has evidence that *DDX3Y* is also expressed in immune cells (5). Moreover, targeted ablation of these genes and their homologues are lethal in yeast, mice, and hematological cell lines (6 - 8). These lines of evidence suggest *DDX3X* and its Y homologue perform highly conserved essential functions in the cell.

Structure & Catalytic Activity

DDX3X belongs to the DEAD box RNA helicase family within helicase superfamily 2 (9, 10). This family of helicases are highly conserved and are characterized by a conserved amino acid sequence, Asp-Glu-Ala-Asp (DEAD). DEAD box RNA helicases contain a catalytic core of two RecA-like domains with nine total conserved motifs: Q motif, motif 1, 1a, 1b, II, III, IV, V, and VI. DEAD box RNA helicases bind and catalyze RNA complexes and ATP in the cleft between the RecA like domains as mediated by the motif residues. DDX3X recognizes

RNA:RNA and RNA:DNA duplexes containing a single-stranded tail, preferentially a 3’ tail (6). Using the single-stranded tail to load onto the duplex, DDX3X binds to the RNA and, stimulated by ATP binding, unwinds the strands through local strand separation as opposed to translocation. Approximately 10 base pairs, or two helical turns, are destabilized at a time. RNA binding stimulates ATP hydrolysis whereupon ADP binding promotes dissociation of DDX3X from either the duplexed substrate or unwound product. Remaining duplexed substrate will be re-bound by DDX3X until productive strand separation occurs, thus ATP hydrolysis drives strand separation by enzyme recycling instead of driving strand separation activity itself.

Molecular & Cellular Function

DDX3X has both catalytic and non-catalytic roles throughout RNA metabolism. DDX3X has been shown to function as a transcription factor subunit (eg. Sp1) for p21 (11, 12). DDX3X has a suggested role in splicing due to the presence of an RS-like domain and is distributed in nuclei as nuclear speckles, both features being associated with splicing factors (Kellie Rosinski dissertation). However, this function is still largely unexplored. In contrast, DDX3X is a well characterized RNA export factor via the CRM1-dependent export pathway (Kellie Rosinski dissertation; 13). Accordingly, DDX3X and its RNA cargo are restricted to the nucleus upon small molecule inhibition of CRM1 by leptomycin B. The interaction between DDX3X and CRM1 is mediated by L19 and L21 (14). DDX3X may also passively exit the nucleus as neither CRM1 inhibition nor mutagenesis of L19/L21 completely ablate DDX3X export. Finally, DDX3X has well-characterized roles in the cytoplasm, predominantly acting as a translational regulator of several transcripts (15 - 17). A major rate-limiting step in gene expression is the unwinding of complex 5’ UTR mRNA regions that otherwise obscure the start codon from translational machinery. However, only the translation of a subset of DDX3X-associated transcripts has been confirmed to be regulated by DDX3X (eg. Cyclin E). During times of stress, DDX3X forms and regulates punctate cytoplasmic foci in association with markers of stress granules - membraneless organelles that are believed to protect transcripts from damage and degradation (17, 18). Apart from its role in the metabolism of protein-coding RNA, DDX3X is also found to be important for the biogenesis of non-coding RNA species such as miRNA and rRNA (19, 20). Moreover, DDX3X is specifically localized to sites of rRNA transcription, the nucleoli, as visualized by both immunofluorescence microscopy and live cell imaging (Chapter 2). Thus, DDX3X participates in a number of RNA processing steps essential for cell survival.

Roles in Human Disease

Development

In mammals, disruption of *DDX3X* affects early development. A murine germline *Ddx3x* knockout model found an accumulation of DNA double-strand breaks and subsequent apoptosis in early murine development (7). In humans, hypomorphic germline variants of *DDX3X* result in a myriad of neurodevelopmental symptoms collectively known as “DDX3X syndrome” in females or intellectual disability in males (21). The pathogenesis of these diseases is unknown, but mutations in *DDX3X* appear to reduce helicase activity (22, 23). Furthermore, recent evidence suggests that germline *DDX3X* mutations predispose affected individuals to cancer (24). Indeed, somatic mutation of *DDX3X* is heavily associated with cancer, as is dysregulated expression.

Cancer Biology

DDX3X is a major cancer-associated gene. *DDX3X* is significantly mutated in solid tumors such as skin (1-5%), oral (10%), head & neck (4%), and medulloblastoma (20%, 50% WNT-subtype), but is most frequently mutated in hematological cancers such as T-cell acute lymphoblastic leukemia (3% overall, 30% of *MLTT10* translocation$_{+}$ cases), chronic lymphocytic leukemia (3-15%), NK/T cell lymphoma (20%), and Burkitt lymphoma (30-50%) (25 - 32). Predicted loss of function mutations are enriched in blood cancers relative to solid. Intriguingly, an unbiased analysis of exome sequencing data from over 4,000 cancers and 21 cancer types revealed a male mutational bias in *DDX3X* (33). Furthermore, *DDX3X* is overexpressed in several solid cancer types and cell lines including Ewing sarcoma, prostate cancer, breast cancer, etc., and under-expressed in colorectal cancer (34, 35). Cases of both over- and under-expression are reported for lung and liver cancer. These diverse routes of *DDX3X* disruption have led to a number of proposed oncogenic and tumor suppressive mechanisms including, but not limited to, roles in WNT signaling (36), EMT transition (37, 38), p53 stabilization (39), hyper stress-granule assembly (18), transcription of p21 (12), translation of MITF (40), regulation of E-cadherin (41), and the regulation of oncogenic miRNA (42).

DNA Repair

Overview of DNA damage & repair

DNA is constantly exposed to endogenous (eg. spontaneous oxidation, deamination, methylation, etc.) and exogenous (UV irradiation, environmental chemicals, etc.) sources of damage (43). These sources create a diverse array of DNA lesions each with an associated DNA repair pathway. Small lesions such as single-strand breaks and base oxidations (eg. 8-oxoguanine) are repaired by the related pathways of single-strand break repair (SSBR) and base excision repair (BER). Briefly, damaged bases are specifically detected by a sensor protein (eg. 8-oxoguanine by OGG1) and then excised from the associated deoxyribose. This abasic site is then hydrolyzed from the sugar-phosphate backbone leaving a nick on one DNA strand. An undamaged nucleotide is then resynthesized into the nick and re-ligated to the backbone. Bulky lesions, such as intrastrand crosslinks (eg. pyrimidine dimers), are similarly repaired by the nucleotide excision repair pathway (NER), but with a larger patch of nucleotides containing the lesion being excised and replaced. Finally, interstrand crosslinks will block DNA replication machinery, thereby prompting a cascade of FANC proteins (eg. FANCA, FANCB, etc.) to sense and remove the crosslink, replace the base pairs, and restart DNA replication in a pathway known as the Fanconi anemia repair pathway or interstrand crosslink repair pathway.

While NER is traditionally associated with having a dedicated transcription-coupled repair pathway (44), virtually all repair processes have demonstrated transcription-associated steps (45, 46). This connection between transcription and repair is the impetus for current research trying to understand the role of RNA in DNA repair, the majority of which is centered on DNA double-strand breaks (DSBs) and its associated repair pathways.

Double-Strand Break Repair

DSBs are the most toxic type of DNA damage. One DSB is sufficient to trigger cell death if left unrepaired (47). Yet, DSBs are also programmed in the process of meiotic recombination in gametes and antigen receptor diversification in lymphocytes (48, 49). Dysregulated repair of either ectopic or programmed DSBs can lead to gross chromosomal alterations such as translocations that can drive oncogenesis (50). Two highly conserved major pathways are utilized to repair DSBs: classical non-homologous end joining (cNHEJ) and homology directed repair (HDR) or homologous recombination. In humans, cNHEJ is the dominant repair pathway.

cNHEJ is active throughout all phases of the cell cycle, most prominently in G_0 and G_1 (51). Upon break induction, the Ku70/Ku80 heterodimer (Ku complex) rapidly associates to the exposed DNA ends. The Ku complex serves as a tether to hold broken ends together in a complex with DNA-PKcs which threads the exposed DNA ends through a channel and displaces the Ku complex along the DNA. While the role of DNA-PKcs in cNHEJ is still unclear, its best characterized activity is the extensive auto phosphorylation and phosphorylation of several other repair factors that occur upon DSB binding which is thought to stimulate and regulate DNA repair activity. The Ku complex also serves as a scaffold for the other requisite repair factor, LIG4, and its accessory proteins. 'Clean' ends can be directly ligated together by LIG4. For 'dirty' ends, processing factors are recruited by the Ku-DNA-PKcs-LIG4 complex to chemically modify the damaged DNA ends to contain ligatable 5' phosphate and 3' hydroxyl groups and/or contain bases for base-pairing. While cNHEJ is not inherently error-prone, extensive processing of DNA ends may cause the formation of small indels.

In contrast, HDR utilizes a homologous template generated during DNA replication to reconstitute the broken DNA sequence (51). As such, this pathway is active in the S and G_2 phase of the cell cycle and negatively regulates cNHEJ machinery. Once detected by the MRN complex (Mre11a, Rad50, NBS1), BRCA1 promotes the short-range resection of DNA ends by first MRN and CtIP 5' exonuclease activity, then Exo1 for long range resection to generate 3' single-stranded DNA ends (ssDNA). The long, exposed ssDNA is coated by RPA for protection and to resolve ectopic secondary structures. BRCA2 then loads Rad51 onto ssDNA to generate recombinogenic nucleofilaments that initiate a homology search for a suitable template. Once bound to a sufficient template, primed DNA synthesis occurs from the resected DNA end. Newly synthesized ends are re-annealed and ligated back to their original position.

RNA-related Repair

Recent research has suggested that RNA may play an important role in the process of DNA repair, namely of DSBs. RNA:DNA hybrids and long-non coding RNA species have been found to accumulate upon break induction as detected by ChIP-Seq, strand-specific RT-PCR, and live cell imaging (52 - 54). While bulky lesions and repair machinery can cause RNA polymerase backtracking and subsequent ectopic RNA:DNA hybrid formation, the bi-directional formation of these hybrids suggest they are, at least in part, synthesized *de novo* or formed from pre-existing RNA in a programmed response (55). In *Schizosaccharomyces pombe*, the degradation of RNA:DNA hybrids causes hyper-resection during DSB repair, suggesting RNA may be used to regulate resection by hybridizing with ssDNA generated during HDR (56). Additionally, RNA has been implicated to play a pro-repair function in cNHEJ. Mammalian cells displayed the ability to use transcribed RNA to serve as a template for DSB repair dependent on cNHEJ factors (57). The localization of 53BP1 to sites of breaks is sensitive to RNase digestion and colocalizes with DNA damage-induced long non-coding RNA species in mouse embryonic fibroblasts (53, 58). Additionally, proteins that process RNA species, Dicer, Drosha, Senataxin, Aquarius, and DDX1 are important for DSB repair (59 - 64). Finally, a number of RNA-binding proteins are recruited to sites of DNA damage in a PARP1-dependent manner including NELF-E, NONO, FUS, CIRBP, hnRPUL1, Rpp29, Rpp21, and RBM14 (65 - 71). Collectively, this suggests that RNA plays an integral and programmed role in the repair of DNA damage.

Implications in Health & Disease

Understanding the function of the DNA damage response (DDR) and DNA repair is of great importance to the biomedical community. Germline and somatic mutations in genes encoding DNA repair proteins are highly associated with disease (43). Major examples of germline mutations in DDR and repair genes include *LIG4*, *FANC* genes, and *BRCA1/2* which cause immunodeficiency, neurodevelopmental issues, and/or a predisposition to cancer. Accordingly, such acquired mutations are frequently found in various cancer tissue types. This phenomenon suggests genomic instability is a key step in carcinogenesis that promotes the acquisition of necessary cancer-promoting mutations (72). Furthermore, this increased rate of mutagenesis also generates clones resistant to cancer therapies. Fortunately, complete loss of DDR and repair capabilities is lethal, thus DNA repair-deficient cancers are vulnerable to targeted therapies that inhibit specific dependent pathways. Characterizing the specific DDR and repair deficiencies caused by mutations is essential in understanding the pathogenesis and treatment of numerous diseases, namely cancer.

Lymphocyte Development

Recent *Ddx3x* knockout male murine models display deficiencies in generating immune cells. The B-cell lineage is particularly affected by *Ddx3x* deficiency concomitant with reduced antibody class diversity. As antigen receptor generation is a DSB repair-dependent process, we hypothesize that the relationship between DDX3X and DSB repair may be important for immune cell development, in part, through antigen receptor recombination (Ch. 3).

Overview of Hematopoiesis

Hematopoiesis is the process by which hematopoietic stem cells (HSCs) differentiate and give rise to blood cells (73). HSCs reside in the bone marrow and contain unlimited self-renewal capacity. At steady-state, HSCs are largely quiescent with their activity regulated by both cell intrinsic and extrinsic factors. Self-renewal capability and pluripotency are intrinsically maintained by a set of transcription factors. Such transcriptional programs are extrinsically maintained or altered by interactions with the stem cell niche in the bone marrow. HSCs are localized near vasculature in the bone marrow and are regulated by a number of cell types including progeny cells like macrophages, megakaryocytes, and regulatory T cells as well as structural cells including adipocytes, sympathetic nerve cells, nonmyelinating Scwann cells, endothelial, and perivascular cells. HSCs undergo asymmetric division to generate multipotent progenitors with the capability of generating common myeloid progenitors (CMPs) and common lymphoid progenitors (CLPs). CMPs differentiate into erythrocytes and innate immune cells such as megakaryocytes, macrophages, and neutrophils. CLPs differentiate into B, T, and NK cells. As HSCs differentiate, daughter cells migrate to different niches of the bone marrow that promote specific lineages through receptor and cytokine interactions. For example, lymphoid progenitors are localized near bone and interact with osteolineage cells to promote lymphopoiesis.

Lymphopoiesis

CLPs differentiate into B and NK cells within the bone marrow while CLPs that have migrated to the thymus differentiate into T cells (74). B cell development is largely driven by the expression of the transcription factors, Pax5 and EBF1, which repress myeloid and T cell transcriptional programs and promote B cell-specific gene expression. For example, Pax5 upregulates pre-BCR signaling components to support pre-B to immature B cell stage progression. Alternatively, CLPs begin T cell development through Notch signaling via interactions with thymic cells. Both lymphocyte development stages are characterized by the expression of RAG1/2 which trigger and direct recombination at the V, D, and J gene segments of the B cell receptor or T cell receptor loci (75). RAG1/2 induce DSBs at recognition site sequences that flank V, D, and J segments which will undergo cNHEJ-mediated joining of the broken segments, resulting in an interstitial deletion. Upon B cell commitment, pro-B cells will first recombine D and J gene segments on the BCR heavy chain loci followed by V and DJ rearrangement. Productive rearrangement of the heavy chain will generate a pre-BCR. Finally, pre-BCR signaling will induce rearrangement of the light chain V and J segments in this pre-B cell stage to ultimately produce a productive BCR on the cell surface. However, up to 50% of nascent BCRs are autoreactive (76). Autoreactive BCRs will predominantly cause RAG reactivation and initiate secondary light chain recombination to generate non-autoreactive BCRs.

BCR^{+} cells will exit the bone marrow as immature B cells to complete development in secondary tissues (77). Upon successful BCR:antigen binding in germinal centers in the lymphatic periphery, BCR affinity is enhanced by targeted mutagenesis by AID in a process called somatic hypermutation (SHM). AID catalyzes the conversion of cytosine to uracil in the antigen interacting region of the BCR (CDR3 region) which triggers BER and MMR to eventually introduce a mutation. The transcription factor, c-Myc, is expressed in bursts during this editing process to promote proliferation of antigen-specific clones. Upon the generation of high-affinity BCRs, the edited B cells will secrete their immunoglobulin as antibodies and undergo class switch recombination (CSR) to generate different classes of antibodies which differ in their constant region. B cells that have undergone somatic hypermutation and class switch recombination to generate high affinity BCRs mature into memory B cells which are sustained for decades and can be re-stimulated as a secondary response to infection.

Chapter 2

DDX3X plays a multifactorial role in DNA DSB repair

Sections of this chapter are adapted from a manuscript in preparation.

Cargill, M.J., Morales, A.J., Ravishankar, S., and Warren, E.H. DDX3X plays a multifactorial role in DNA DSB repair.

Abstract

Recent studies have suggested that DDX3X plays a role in DNA repair. We aimed to investigate the hypothesis that DDX3X plays a multifactorial, RNA metabolism-related role in DNA repair. Protein identification and quantification by mass spectrometry identified several DNA repair proteins sensitive to DDX3X disruption. Colocalization and co-immunoprecipitation analysis *in vitro* revealed interactions with DNA repair factors, namely γH2AX and 53BP1. Indeed, DDX3X was recruited to sites of microirradiation *in vivo* in a PARP1-dependent manner which was found to be mediated through the intrinsically disordered domains at the N- and C-termini. DDX3X interacts extensively with RNA-related factors such as RNA polymerase II and RNA-binding proteins and is likewise dependent on transcription for recruitment and regulating γH2AX induction upon DNA damage. Inhibition of DDX3X activity reduced global, co-transcriptional, and DSB-induced DNA:RNA hybrid levels, but did not affect DSB-induced transcriptional repression in *RBMXL1* - the model gene that undergoes DNA:RNA hybrid formation upon DSB induction. Interestingly, DDX3X inhibition promoted dsRNA formation at the *AsiSI* site in *RBMXL1*. Finally, both major DSB repair pathways were sensitive to DDX3X manipulation. In particular, we found the role of DDX3X in end-joining repair to be dependent

on Ku70, implying DDX3X operates in the classical non-homologous end joining pathway. Thus, DDX3X plays a multifactorial role in DNA DSB repair.

Introduction

The deep connection between *DDX3X* and human disease (e.g., cancer and viral infection) has made DDX3X a prime therapeutic target. Recent studies evaluating the effects of small molecule inhibition of DDX3X revealed an intriguing link between this RNA helicase and DNA repair (34, 78, 79). Upon small molecule inhibition or siRNA knockdown of DDX3X, human cancer cell lines become radiosensitive, accumulate DNA breaks, and have reduced DNA DSB repair efficiency as determined by colony formation assay, γH2AX immunofluorescent staining, and fluorescent reporter assays respectively. Orthogonal studies further support the relationship between DDX3X and DNA repair. *Ddx3x* knockout mouse models similarly accumulate DNA breaks in early developmental stages while a human DEAD box RNA helicase, DDX1, directly supports DNA DSB repair (7, 63, 64).

The emerging role of RNA-interacting proteins, such as DEAD box RNA helicases, in DNA repair remains largely unknown. The vast majority of these proteins promote gene expression, the dysregulation of which may indirectly impact DNA repair by altering steady-state DNA damage response and repair (DDR) protein levels (80). Alternatively, a subset of RNA-interacting proteins is also known to directly support DNA repair in two capacities: transcriptional repression and damage-induced RNA metabolism. Classically, this subset promotes transcription termination and is, thus, recruited to evict RNA polymerase and resolve ectopic RNA-containing structures due to RNA polymerase stalling at DNA lesions in an actively transcribed gene (81, 82). Damage-induced RNA biogenesis and processing is an emerging, but highly conserved, molecular process that is predominantly associated with DSBs

(83). Such damage-induced RNA species include microRNA and RNA:DNA hybrids, yet it remains unclear whether novel damage-induced RNA species are synthesized *de novo* or are recycled from pre-existing transcripts. A multitude of pro-repair functions have been described where RNA serves as a DNA damage signal, a protein regulator, DNA resection inhibitor, and as a repair template (Chapter 1, 84). Thus, we hypothesized that DDX3X plays a multifactorial role in DNA DSB repair by regulating DDR protein levels and RNA metabolism at DSB sites.

Methods

Cell culture and cell line generation

HEK293T cells (ATCC) and the U2OS-DIvA cell line (DIvA; a gift from Gaelle Legube) were cultured in Dulbecco's Modified Eagle Media (DMEM) supplemented with 10% FBS, L-glutamine, and pen/strep with the DIvA cell additionally cultured in the presence of 1 µg/mL puromycin. *AsiSI*-induced DSBs were generated by treating DIvA cells with 300 nM 4-hydroxytamoxifen (OHT) for 4 hrs (85). The HEK293T-TLR cell line was created by generating Traffic Light Reporter (TLR; a gift from Nancy Maizels, University of Washington, Department of Immunology) containing lentiviral particles with a third generation packaging system, concentrating the virus according to the Lenti-X concentrator manufacturer's protocol (Clontech), then transducing HEK293T cells overnight at a ~ 20% confluency in 8 µg/mL polybrene and selected with 2 µg/mL puromycin for 72 hrs. The *PARP1* knockout HEK293T cell line was generated by transfecting (as described below) 1.6 µg pCas9-BFP, 200 ng psgPARP1-3, and psgPARP1-4, then sorting BFP+ cells on a BD FACS Aria followed by single cell isolation in a 96 well plate. PARP1-deficient clones were screened by western blot as described below.

Plasmid construction

pDDX3X-GFP was generated by Kellie Rosinski as described in her archived dissertation. The iRFP-tagged constructs were generated via Gibson assembly using PCR-amplified cDNA inserts and *MunI*- and *Bpu*-digested pmiRFP670. Codon-optimized DDX3X-HA was custom synthesized by GeneArt (Thermo Fisher) and cloned into the pcDNA3.1 expression vector. Point mutant derivatives of pcDNA3.1-DDX3X-HA and pDDX3X-GFP were generated via the QuickChange II XL Kit (Agilent) as described by the manufacturer's protocol using HPLC-purified oligos (IDT; Reagents table). Deletion constructs were generated by PCR-amplifying the indicated fragments of pDDX3X$_{L19A/L21A}$-GFP, then inserted into *EcoRI*- and *XbaI*-digested pEGFP via Gibson assembly following the manufacturer’s protocol (Ch. 2 Reagents Table). Guide RNA expression vectors targeting *DDX3X* and *PARP1* were constructed by annealing oligos (IDT) encoding the target sequences (Ch. 2 Reagents Table) and inserting into the pMLM3636 vector following the depositor’s protocol (Addgene). All constructs were extracted from transformed bacteria via miniprep plasmid extraction (Qiagen) and verified by Sanger sequencing.

Transfections

All cDNA and reporter transfections were performed using Lipofectamine LTX transfection reagent according to the manufacturer’s protocol with 2.5 µL LTX (< 1000 ng DNA) or 5 µL LTX (< 1000 ng DNA) in 200 µL OptiMEM (Thermo Fisher) per 1 mL antibiotic-free DMEM with HEK293T cells at 20-40% confluency. All cells in transfection-based assays were measured 72 hrs post-transfection. Transient knockdowns were performed using 5 µL Dharmafect transfection reagent (Dharmacon) with 50 nM pooled siRNA (Dharmacon; resuspended in 1X siRNA buffer) in 1 mL antibiotic-free DMEM (12-well plate) with HEK293T cells at ~ 60-70% confluency. Knockdowns were verified by western blot 72 hrs post-transfection.

Western blot

Whole protein was extracted from cell pellets by adding 1 mL/ 10 million cells RIPA lysis buffer (Thermo Fisher) freshly supplemented with protease inhibitors (Pierce), nutating at 4 °C for 30 min, centrifuging at 14,000 G, and harvesting the supernatant. Protein concentration was determined by BCA assay (Pierce). Approximately 8 - 10 µg of protein per sample was boiled in 1X Laemmli buffer at 95 °C for 5 min, then loaded onto NuPAGE 10% Tris-bis gel (Thermo Fisher; protein target < 200 kDa) in 1X MOPS-SDS running buffer or NuPAGE 4-12% Tris-acetate gel (Thermo Fisher; protein target > 200 kDa) in 1X Tris-acetate running buffer for gel electrophoresis. After gel electrophoresis, protein was transferred onto a nitrocellulose membrane using the iBlot transfer kit according to the manufacturer's protocol. The membranes were blocked by nutating in 5% BSA (PBST) for one hour at room temperature. Blocked membranes were stained with the indicated primary antibodies by nutating in 5% BSA (PBST) overnight at 4 °C followed by IRDye secondary antibody staining by nutating in 5% BSA (PBST) for one hour at room temperature. Membranes were washed three times for 5 min with PBST after each antibody staining. Blots were imaged on a Licor Odyssey scanner at 700 nm and 800 nm.

Nuclear Co-immunoprecipitation

Co-immunoprecipitation was performed on HEK293T nuclear extracts with anti-DDX3X or polyclonal rabbit IgG following the manufacturer's protocol of the Nuclear Content IP kit (ActiveMotif) without vortexing. Briefly, 10 million cells were washed in ice-cold PBS supplemented with phosphatase inhibitors and incubated in hypotonic buffer, then lysed with detergent. Nuclei were pelleted and resuspended in an enzymatic cocktail for digestion at 4 °C for 90 min prior to re-centrifugation. Nuclear protein content was harvested from the supernatant. Nuclear protein content from 20 million cells (~ 400 - 500 µg protein) was incubated overnight at 4 °C in 1X low IP buffer with 4.5 µg antibody. Protein:antibody complexes were column isolated then eluted and boiled in 2X Laemmli buffer. Co-immunoprecipitated protein isolates were loaded onto NuPAGE 10% Tris-bis gels and run in 1X MOPS-SDS running buffer. DDX3X co-immunoprecipitation was verified by western blot targeting hnRNPK, a known nuclear interactor (Supplemental Figure 2.1B).

Mass Spectrometry

Whole proteome quantification was performed as in ref. 86 by the Fred Hutchinson proteomics core from siDDX3X and siNeg knockdown HEK293T cell pellets. Samples were analyzed on a ThermoScientific Orbitrap Eclipse mass spectrometer equipped with FAIMS, field asymmetric ion mobility spectrometry, configured for MS2 quantification. Proteins were identified and quantified using Proteome Discoverer v2.4.

Co-immunoprecipitated protein samples were prepared for mass spectrometry as gel slices. After gel electrophoresis, protein bands were visualized by SimplySafe Blue Coomassie (Thermo Fisher) staining for one hour, followed by two one-hour washes in deionized water all at room temperature with gentle agitation. Gel slices were prepared by excising five regions per sample (excluding Ig heavy and light chains), placed in sterile 2 mL microcentrifuge tubes, then submitted to the proteomics core for mass spectrometry. Briefly, protein was released from the gel matrix, then proteolytically digested and desalted prior to being run on an Orbitrap Fusion mass spectrometer for protein identification by LC-MS/MS. Protein spectra were annotated and filtered at a 1% false discovery rate using Proteome Discoverer v2.4. Protein hits that were below statistical significance ($p < 0.01$) and/or had less than 10 peptide spectral matches (PSMs) in the anti-DDX3X samples were removed. The remaining protein hits were delineated as either enriched (anti-DDX3X/ IgG ratio > 1; or exclusive to the anti-DDX3X fraction) in one or both experiments. All protein hits depleted (< 1) in the anti-DDX3X fraction in either experiments were removed. Proteins displayed in Figures 2.2, 2.4, 2.5, and 2.6, were selected from the resulting protein list, with proteins enriched in both experiments in bold. The resulting protein list was also analyzed with DAVID 6.8 to determine pathway enrichment as defined by gene ontology biological pathway (GO-BP) terms.

Immunofluorescence

For 3D imaging, cells were grown to ~ 50% confluency on a poly-L-lysine coated #1.5 coverslip. For irradiation, HEK293T cells were gamma irradiated at 5 Gy four hours (γH2AX) or two hours (53BP1) prior to permeabilization. In order to remove the cytoplasmic signal, cells were first permeabilized in 0.5% Triton X-100, fixed in 2% paraformaldehyde for 20 min, then washed once with ice-cold PBS. Coverslips were blocked in 3% BSA (PBST) for 30 min followed by one wash with PBST. Coverslips were then stained with the indicated primary antibodies overnight at 4 °C while nutating (Reagents table Ch. 1) in 3% BSA (PBST), then stained with the indicated secondary antibodies for one hour at room temperature, with three 5 min PBST washes after each antibody incubation. For DDX3X staining only, cells were similarly stained with 1% BSA in PBS. Coverslips were incubated with 1 µg/ mL DAPI in distilled water for 1 min then mounted with Gold Antifade Mountant (Thermo Fisher) on Apex slides (Leica) to cure overnight at room temperature. Slides were imaged with Z-stacks at 0.2 mm intervals in the Fred Hutch Cellular Imaging core on the Deltavision elite microscope. Z-stacks were deconvolved and rendered in Imaris for analysis.

For high throughput imaging, cells were grown to ~ 50% confluency in flat-bottom 96 well plates (Biolite) with poly-L-lysine coating for HEK293T cells. Cells were stained as previously described and imaged on the ImageXpress microscope in 100 µL PBS. The integrated intensity per nucleus was calculated from the DAPI signal.

Live cell imaging

HEK293T cells were transfected as described and seeded into poly-L-lysine coated 35 mm Nunc glass bottom dishes 24 hours later. Prior to imaging, cells were stained with 10 µg/ mL Hoechst 33342 for 10 min, then cultured in phenol red-free DMEM. Using an Ultraview Spinning Disk microscope, cells were imaged (488 nm, 640 nm) every 5 seconds and micro-irradiated (15%, 405 nm) after 20 seconds. Exported videos were analyzed on ImageJ using the ROI function to measure intensity over time relative to a non-irradiate ROI when indicated or fold change relative to pre-irradiated intensity.

Flow cytometry

For the TLR assay (87), transfected cells were washed with PBS, pelleted, and resuspended in MACS running buffer. Samples were analyzed on a BD FACS Symphony to measure BFP$_+$ (Pacific blue; 405 nm), mCherry$_+$ (PE-mCherry; 552 nm), and GFP$_+$ (FITC; 488 nm) events. Using FlowJo software, repair efficiency was calculated for BFP$_+$ singlet events as the frequency of mCherry$_+$ (EJ) or GFP$_+$ (HDR) events relative to the indicated control (Supplemental Figure 2.2).

For the flow retention assay (88), transfected cells were pelleted, permeabilized in 0.05% Triton X-100 supplemented with protease inhibitors (Pierce) in PBS for 4 min, then fixed in 2% paraformaldehyde for 20 min and stained with 1 µg/ mL DAPI all at room temperature. Nuclei were analyzed on a BD FACS Symphony to measure DAPI$_+$ (Pacific blue; 405 nm) and miRFP$_+$

(APC; 628 nm) events and analyzed with FlowJo software. Relative retention was calculated as the mean fluorescent intensity (MFI) of miRFP$^+$ events subtracted from the miRFP$^-$ population MFI relative to indicated controls among G$_0$/G$_1$ phase, DAPI$^+$ singlets.

DNA:RNA Hybrid Immunoprecipitation (DRIP)

DIvA cells were grown to ~ 80 - 90% confluency in 10 cm dishes. Genomic DNA was extracted following the manufacturer's protocol using the QIAmp DNA blood mini kit (Qiagen) without vigorous vortexing. Approximately 4 - 5 µg of gDNA was digested overnight at 37 °C with 20 units each of EcoRI, HindIII, BsrGI, and XbaI (New England Biolabs) in 1× NEBuffer 2 diluted in Ultrapure water (Thermo Fisher). Digested gDNA was purified with a Purelink PCR purification kit (Thermo Fisher). Protein A dynabeads (Thermo Fisher) were blocked with 0.5% BSA (PBS) for one hour while nutating. Using a magnetic stand, blocked beads were then washed twice with 0.1% Triton X-100 in PBS (IP buffer). The beads were coated while nutating with 10 µg of S9.6 or IgG2 isotype control for four hours at 4 °C and washed once with IP buffer to remove excess antibody. Approximately 3 - 5 µg of purified, digested gDNA was incubated with antibody-coated dynabeads in 500 µL IP buffer supplemented with 5 nM EDTA overnight at 4 °C while nutating. Approximately 15% of the purified, digested gDNA was reserved as input template DNA. After incubation, dynabeads were washed twice with IP buffer for 10 minutes at room temperature, then resuspended in 100 µL of IP buffer to be digested with 10 µg of proteinase K (Thermo Fisher) for 45 minutes at ~ 55 °C. The dynabeads were then pelleted and the supernatant containing immunoprecipitated DNA was harvested and re-purified with a Purelink PCR purification kit.

RNase I$_f$ Digestion and Reverse Transcription

For the RNase I_f RT-qPCR assay (89), RNA was extracted from DIvA cells with the RNeasy Mini Kit (Qiagen) with DNase I digestion followed by RNase I_f (NEB) digestion of 500 ng RNA according to the manufacturer's protocol. Digested RNA was re-purified with the RNeasy Mini Kit. Samples were pre-heated at 95 °C for 5 min prior to reverse transcription with the RNA to cDNA High Capacity Kit (Thermo Fisher). 10% of the reaction was used for qPCR.

qPCR

Quantitative PCR was performed using Platinum SYBR QPCR Supermix w/ ROX (Thermo Fisher) following the manufacturer's protocol using MicroAmp Optical 96 well plates. PCR reactions were monitored using ABI QuantStudio5 Real Time PCR systems and analyzed on QuantStudio using a Ct threshold of 0.4. Primer sequences are available in the reagents table (Ch. 2 Reagents Table).

Cut&Run Sequencing

All steps were performed at room temperature. Treated cells were washed three times in 1 mL of wash buffer (20 mM HEPES pH 7.5, 150 mM NaCl, and 0.5 mM spermidine in the presence of protease inhibitors in Ultrapure water), then resuspended in 1 mL wash buffer. Concanavalin beads (10 uL/ sample) were activated by washing twice with activation buffer (20 mM HEPES pH 7.5, 10 mM KCl, 1 mM $CaCl_2$, 1 mM $MnCl_2$ in Ultrapure water) by gentle inversion. Activated concanavalin beads were added to washed cells with gentle agitation then incubated for 10 min while nutating. Cell:bead complexes were then aliquoted to 0.2 mL tubes at a ratio of 400,000 cells per 10 µL of beads, pelleted by magnetic stand, and resuspended in antibody buffer (0.05% digitonin, 2 mM EDTA in wash buffer). Rabbit primary antibodies were added as indicated (Ch. 2 Reagents table) and incubated overnight at 4 °C while nutating.

After overnight antibody incubation, the samples were processed by the Cut&Run automated service (autoCut&Run) by the Fred Hutch genomics core (90). Samples were arrayed in a 96 well plate, then incubated with protein A/G-MNase fusion protein (700 ng/ mL) for one hour at 4 °C to allow binding, then washed twice with digitonin wash buffer (0.05% digitonin). The Protein A/G domain allows the fusion protein to selectively bind to the indicated rabbit antibodies. MNase cleavage of local genomic regions is initiated with 100 mM $CaCl_2$ incubated for 9 min at 0 °C, then quenched with STOP buffer (80 mM EGTA, 0.05% digitonin, 100 µg/ mL RNase A) spiked with heterologous yeast DNA (0.2 pg/ µL). Digested chromatin underwent DNA end-repair and dA-tailing with ERA buffer (4X T4 DNA ligase buffer, 2 mM dNTPs, 1 mM ATP, 10% PEG 4000, 0.5 U/ µL T4 PNK, 0.05 U/ µL T4 DNA polymerase, 0.05 U/ µL Taq DNA polymerase) using a four-step program: 12 °C 15 min, 37 °C 15 min, 58 °C 1.5 hours, 8 °C hold. Pre-annealed adaptor oligos were ligated in ligase solution (2X Enzymatics Rapid DNA ligase buffer, 10% Enzymatics DNA ligase) with 15 nM of adaptor oligos for 20 min at 20 °C, then immediately digested with Proteinase K (Thermo Fisher) as per the manufacturer’s protocol. Ligated DNA underwent two rounds of Ampure bead clean-up using an automated Biomek deck with the following reagent set-up for plates 1 - 9 (in order as follows): V-bottom plate with 100 µL 10 mM Tris-HCl pH 8, V-bottom plate with 100 µL 10 mM Tris-HCl pH 8, ALPAQUA magnet plate, deep well plate with 1 mL 80% ethanol, PCR 96 well plate containing 110 µL of adapter ligated sample DNA stacked on a PCR plate rack, PCR 96 well plate with 90 µL of ampure beads stacked on a PCR plate rack, V-bottom plate with 100 µL HXP mix (20% PEG 8000, 2.5 M NaCl), PCR 96 well plate for accepting cleaned-up DNA stacked on a PCR plate rack, deep well plate for receiving liquid waste. Sample DNA was PCR amplified with 20 µL KAPA PCR master mix (2.5X KAPA buffer, 0.75 mM dNTPs, 5 µM P5 primer, 5 µM P7 primer, 10% KAPA HS HIFI polymerase) with the following PCR program: 98 °C 45 sec, 14X 98 °C 15 sec, 14X 60 °C 10 sec, 72 °C 1 min, 8 °C hold. PCR products were re-purified with 55 µL Ampure beads using the aforementioned Biomek deck set-up. Purified PCR products containing sample-specific indices were pooled and assessed by Agilent TapeStation analysis prior to paired-end sequencing on an Illumina Miseq instrument.

Bioinformatic analysis was performed by Dr. Shashidhar Ravishankar. FASTQC and BBDuk were used for quality control of the raw fastq files where reads with average quality less than 30 were removed. The remaining reads were aligned to the *Saccharomyces cerevisiae* spike-in genome reference, sacCer3, to determine the abundance of spike-in reads for each sample. The normalization factor was based on the lowest spike-in abundance among all samples. Reads were then subsampled based on the normalization factor and aligned to the human reference genome, hg48, using Bowtie2 (`bowtie2 --very-sensitive –dovetail -x $genome_index_path -1 ${read_one} -2 ${read_two} -S ${sample}.sam`). Aligned reads pairs were coordinate sorted and the GATK MarkDuplicates utility was used to remove PCR duplicates. Peak calling was performed using MACS2 from the filtered alignments with the IgG control samples. The $\log_2$ fold change of cut (four hour tamoxifen treatment) over uncut (untreated control) and log likelihood ratio across each indicated antibody was calculated using the bdgcmp function from MAC2. Bigwig files for sample fold change and log likelihood ratio analyses were generated using Bedtools, UCSC-bedClip, and UCSC-bedGraphToBigWig. Finally, average profile plots from raw reads counts and fold change values were generated using Ngsplot and deepTools2.

Statistical analysis

A student's two-sided t-test was performed to determine statistical significance for all experiments unless otherwise specified. * = $p < 0.05$, ** = $p < 0.01$, *** = $p < 0.001$, **** = p <

0.0001. Error bars represent standard error of the mean (SEM) throughout unless otherwise specified.

Ch. 2 Reagents Table

Reagent	**Vendor/ Source**	**Working Amount**	**Sequence (if applicable)**
psgTLR-2	Nancy Maizel Lab	500 ng	
pdonorGFP	Nancy Maizel Lab	300 ng	
pCas9-BFP	Nancy Maizel Lab	500 ng	
pAniI-BFP	Nancy Maizel Lab	500 ng	
pLenti-TLR-Puro	Nancy Maizel Lab	1.5 µg	
pRRev	Addgene	1 µg	
pMD2-G	Addgene	0.5 µg	
pRRE	Addgene	1 µg	
pDDX3X-GFP (and mutant derivatives)	Kellie Rosinski (mutants generated by Michael Cargill)	200 ng	
pmiRFP670	Addgene	--	
pmiRFP670-dRNaseH	Michael Cargill	200 ng	
pmiRFP670-wtRNaseH	Michael Cargill	200 ng	
pmiRFP670-Ku70	Michael Cargill	200 ng	
pmiRFP670-PARP1	Michael Cargill	200 ng	
pICE-dRNaseH-mCherry	Addgene	--	

pICE-wtRNaseH-mCherry	Addgene	--	
pEGFP-Ku70	Addgene	--	
pCMV-3xFLAG-PARP1	Addgene	--	
pcDNA3.1-DDX3X-HA (and mutant derivatives)	GeneArt Thermo Fisher (mutants generated by Michael Cargill)	200 ng (unless otherwise specified)	
pMLM3636 (and guide RNA insert derivatives)	Addgene (guide RNA insert derivatives generated by Michael Cargill)	200 ng	
Quikchange XL II Kit	Agilent	--	
Gibson Assembly Mastermix	New England Biolabs	--	
sgPARP1-1	IDT	--	CGAGTCGAGTACGCCAAG
sgPARP1-3	IDT	--	ACCCTGACGTTGAGGTGGAT
sgDDX3X-2	IDT	--	AACGTGGTGGAAACAGTCGC
sgDDX3X-5	IDT	--	ACCGTAGGTGTCGCGTGCGG
DDX3X-L19A-L21A_F1	IDT	--	GCAGTTTGCTGGCGCAGACGCGAACTCTTCAGATAATCA
DDX3X-L19A-L21A_R1	IDT	--	CTGATTATCTGAAGAGTTCGCGTCTGCGCCAGCAAACTG
DDX3X-L43A_F1	IDT	--	AGATATATCCCTCCACACGCGAGAAACAGAGAGGCCAC

DDX3X-L43A_R1	IDT	--	GTGGCCTCTCTGTTTCTCGCGTGTGGAGGGATATATCT
DDX3X-S382A-T384A_F1	IDT	--	CGGCACACCATGATGTTCGCCGCCGCCTTTCCTAAAGAAATCC
DDX3X-S382A-T384A_R1	IDT	--	GGATTTCTTTAGGAAAGGCGGCGGCGAACATCATGGTGTGCCG
siNeg-Pool	Dharmacon	50 nM	
siDDX3X-Pool	Dharmacon	50 nM	
RNeasy Mini Kit	Qiagen	--	
RNA to cDNA High Capacity Kit	Thermo Fisher	--	
Purelink PCR Purification Kit	Thermo Fisher	--	
QIAmp Blood Mini Kit	Qiagen	--	
Plasmid Miniprep Kit	Qiagen	--	
Effectene Transfection Kit	Qiagen	60 µL / reaction	
Lenti-X Concentrator	Clontech	3 mL / 10 mL supernatant	
Polybrene	Sigma-Aldrich	8 µg/ mL	
Lipofectamine LTX	Thermo Fisher	2.5 - 5 µL (as indicated)	
Dharmafect 1	Dharmacon	5 uL	
5X siRNA Suspension Buffer	Dharmacon	1 X (storage)	
Serum-reduced OptiMEM	Thermo Fisher	200 µL / 1 mL media (12 well dish)	

Nuclear Content CoIP Kit	Active Motif	--	
RIPA Lysis Buffer	Thermo Fisher	1 mL / 10 million cells	
Protease Inhibitor Tablets	Pierce	1 mini tablet / 10 mL RIPA buffer	
NuPAGE 10% Tris-bis gel	Thermo Fisher	--	
20X MOPS-SDS Running Buffer	Thermo Fisher	1X	
NuPAGE 4 - 12% Tris-acetate gel	Thermo Fisher	--	
20X Tris-acetate Running Buffer	Thermo Fisher	1X	
SimplySafe Blue Stain	Thermo Fisher	--	
iBlot Transfer Stacks	Thermo Fisher	--	
BSA (IgG-free)	Sigma-Aldrich	IF: 3% WB: 5% DRIP: 0.5%	
Triton X-100	Sigma-Aldrich	IF: 0.05% DRIP: 0.1%	
Tween 20	Fisher Scientific	0.1%	
#1.5 Coverslips	Thomas Scientific	--	
Prolong Gold Antifade Mountant	Thermo Fisher	--	
DAPI	Thermo Fisher	1 µg/ mL	
Hoechst 33342	Thermo Fisher	10 µg/ mL	
Phenol Red-Free DMEM	Thermo Fisher	--	

Proteinase K	Thermo Fisher	10 ug	
Protein A beads	Thermo Fisher	50 µL / sample	
RNaseH	NEB	5 units	
EcoRI	NEB	20 units	
HindIII	NEB	20 units	
BsrGI	NEB	20 units	
XbaI	NEB	20 units	
NEBuffer 2	NEB	1X	
MunI	Thermo Fisher	3 µL / 5 µg plasmid DNA	
Bpu1102I	Thermo Fisher	3 µL / 5 µg plasmid DNA	
RNase I_f	NEB	50 units / 500 ng RNA	
NEBuffer 3	NEB	1X	
EDTA	Thermo Fisher	Variable	
Rabbit Polyclonal Anti-DDX3X	Abcam	IF: 1:200 WB: 1:5000 CoIP: 5 µg (1 µL)/ 100 µg protein	
Mouse Monoclonal Anti-GAPDH	Abcam	WB: 1:10,000	
Mouse Monoclonal S9.6	Millipore	IF: 1:500 DRIP: 10 µg	
Rabbit Polyclonal IgG Isotype Control	BD Biosciences	5 µg/ 100 µg	
Mouse Monoclonal IgG2 Isotype Control	R&D Systems	10 µg	

Mouse Monoclonal γH2AX	Millipore	1:1000	
Mouse Monoclonal 53BP1	Millipore	1:500	
Mouse Monoclonal Anti-hnRNPK	Abcam	1:1000	
Donkey Anti-Mouse Cy3	Jackson Immunoresearch	IF: 1:2000	
Anti-Rabbit AlexaFlour488	Abcam	IF: 1:200	
IRDye® 680LT Goat anti-Rabbit IgG	LICOR	WB: 1:20,000	
IRDye® 800CW Goat anti-Mouse IgG	LICOR	WB: 1:15,000	
HEPES (1 M)	Thermo Fisher	10 mM	
Digitonin	Millipore	0.05%	
Spermidine	Sigma-Aldrich	0.5 mM	
NaCl	Sigma-Aldrich	150 mM	
$MnCl_2$	Sigma-Aldrich	1 mM	
$CaCl_2$	Sigma-Aldrich	1 mM	
KCl	Sigma-Aldrich	10 mM	
Concanavalin Beads	Bangs Laboratory	10 µL/ 400,000 cells	
RNA to cDNA High Capacity Kit	Thermo Fisher	--	
Platinum™ SYBR™ Green qPCR SuperMix-UDG w/ROX	Thermo Fisher	--	
RBMXL1_Fwd	IDT	200 nM	GATTGGCTATGGGTGTGGAC

RBMXL1_Rev	IDT	200 nM	CATCCTTGCAAACCAGTCCT
RPL13A_Fwd	IDT	200 nM	AATGTGGCATTTCCTTCTCG
RPL13A_Rev	IDT	200 nM	CCAATTCGGCCAAGACTCTA
Puromycin	Sigma-Aldrich	1 - 2 µg/ mL	
Actinomycin D	Thermo Fisher	5 µg/ mL	
Cordycepin	Sigma-Aldrich	50 uM	
4-Hydroxytamoxifen	Sigma-Aldrich	300 nM	
RK-33	Selleckchem	3 µM (unless otherwise indicated)	

Results

DDX3X and the DNA Repair Proteome

DDX3X is an essential human gene that rarely contains homozygous mutations (8), thus endogenous DDX3X levels were knocked-down via siRNA to pathologically-relevant levels of 50% in HEK293T cells. Using mass spectrometry to quantify and identify proteins, we found DNA DSB repair proteins including XRCC4, XRCC3, Nibrin, and Rad51 to be downregulated upon DDX3X knockdown (Figure 2.1A; Appendix Table 1). We verified the DDX3X-dependent nature of the identified DSB repair proteins at the designated statistical significance of 0.05 by measuring Rad51 levels ($p < 0.05$; Figure 2.1B), and XRCC6 levels ($p > 0.05$; Figure 2.1C) via western blot upon DDX3X knockdown. Proteins in other repair pathways were also downregulated including CSB, POLB, and WRNIP. Chromatin remodelers known to be important for promoting DNA repair, CHD2 and SMARCA5, were downregulated (Appendix

Table 1). Finally, repair proteins that were upregulated included XPC, XPD, FANCA, and FANCG . It is important to note that more DNA repair and replication proteins were downregulated (48 proteins) than upregulated (6 proteins). We herein provide the first proteomic evidence that the DNA repair proteome is affected by DDX3X disruption.

DDX3X is associated with DDR proteins

Due to the low nuclear abundance of DDX3X, we utilized mass spectrometry to identify protein interactors of nuclear DDX3X (Appendix Table 2). Co-immunoprecipitation with endogenous DDX3X was detected by enrichment in the anti-DDX3X fraction over the IgG control. Ku70 and DNA-PKcs form the synaptic complex in non-homologous end joining repair and recurrently co-immunoprecipitated with endogenous DDX3X along with SMC3 which is part of the cohesin complex (Figure 2.2A). DDX3X also co-immunoprecipitated with BLM which is associated with recombinatorial DNA repair. Canonical DNA repair factors, PARP1, H2AX and 53BP1 were detected as well, but are likely difficult to detect consistently due to their sizes. We did, however, also detect these proteins enriched in the anti-DDX3X fraction in preliminary mass spectrometry experiments (data not shown).

We further investigated DDX3X nuclear interactions upon DSB formation using immunofluorescence microscopy. HEK293T cells were gamma irradiated and co-stained for DDX3X and two markers of DNA damage found in the coimmunoprecipitation analysis, γH2AX and 53BP1. Three-dimensional imaging of HEK293T nuclei revealed that nuclear DDX3X foci colocalize with a subset of DNA damage markers upon gamma irradiation (Figure 2.2B-G). Interestingly, DDX3X was found to colocalize with endogenous γH2AX foci at nucleolar margins in non-irradiated cells (Supplemental Figure 2.3). Nucleoli are prone to endogenous DSB induction whereupon DNA is reorganized to the periphery for repair (91). Using the DIvA cell line to induce DSBs at *AsiSI* sites throughout the U2OS genome, we found that nuclear DDX3X similarly colocalized with γH2AX (data not shown). It is interesting to note that DDX3X colocalization is RNase sensitive, as is 53BP1 foci formation (Supplemental Figure 2.4; 58). Our *in situ* results suggest endogenous DDX3X plays a direct role in the DNA damage & repair process.

DDX3X is actively recruited to DNA damage in a PARP1-dependent manner

We next employed live cell imaging to evaluate the role of DDX3X in the DNA damage response *in vivo.* Fluorescently-tagged expression vectors for DDX3X and Ku70 were transiently transfected into HEK293T and then pre-sensitized with Hoechst 33342. A nuclear export deficient DDX3X mutant (L19A/L21A) was generated to enhance the recruitment signal. Dual fluorescence imaging upon 405 nm spot microirradiation revealed DDX3X-GFP recruitment to sites of DNA damage as represented by miRFP670-Ku70 (Figure 2.2H). Both DDX3X-GFP and $\text{DDX3X}_{\text{L19A/L21A}}$-GFP recruitment peaks at 90 seconds post-irradiation and dissipates variably between 5 - 10 minutes thereafter (Figure 2.2I).

Numerous RNA-interacting proteins are recruited to sites of DNA damage in a PARP1-dependent manner via an interaction with their intrinsically disordered domains. RNA-binding proteins previously found to be recruited to sites of DNA damage recurrently co-immunoprecipitated with DDX3X including SAFB, RBM14, FUS, NONO, SPFQ, RBMX, and THOC2 which contain intrinsically disordered domains important for recruitment (Figure 2.4A-B; Appendix Table 2). We computationally identified intrinsically disordered domains at the N and C terminus of DDX3X (Figure 2.4C). We explored the hypothesis that DDX3X recruitment activity is similarly regulated. A clonal HEK293T *PARP1* knockout cell line was generated using transient CRISPR/Cas9 expression targeting *PARP1* and subsequent single cell cloning (Figure

2.3A-C). DDX3X$_{L19A/L21A}$-GFP recruitment was abolished in the *PARP1* knockout line which was rescued upon transient re-expression with miRFP670-PARP1 (Figure 2.3D-E). Preliminary experiments inhibiting ATM or DNA-PKcs, other DDR signaling proteins, did not affect DDX3X recruitment (data not shown). Furthermore, deletion of both of the intrinsically disordered domains at the N- and C-termini of DDX3X also ablated recruitment (Figure 2.4D-E). Interestingly, the C-terminal domain alone is sufficient for partial DDX3X recruitment activity. The findings suggest DDX3X is actively recruited to sites of DNA damage in a coordinated response.

The role of DDX3X in DNA repair is transcription-dependent

Similarly recruited RNA-binding proteins regulate transcription at sites of breaks. DDX3X specifically interacts with RNA polymerase II subunits RPB1-3 (Figure 2.5A). DDX3X$_{L19A/L21A}$-GFP recruitment was ablated in cells pre-treated with actinomycin D to inhibit global transcription (Figure 2.5B-C). Furthermore, transcription inhibition also rescued γH2AX induction in DDX3X inhibited DIvA cells upon DSB formation (Figure 2.5D). Importantly, we failed to identify changes in DSB-induced transcriptional repression at the *RBMXL1* locus - the model gene used to measure DSB-induced metabolism in the DIvA cell line (Figure 2.5E; 61). Thus, the role of DDX3X in DNA repair is linked to transcription, but not DSB-induced transcriptional repression.

DDX3X regulates DNA:RNA hybrids

We sought to elucidate the relationship between DDX3X and the major DNA damage-related RNA structure: DNA:RNA hybrids. Using a fluorescently-tagged construct encoding a catalytically-inactive RNaseHI (miRFP-dRNaseHI) to visualize DNA:RNA hybrids, 3D immunofluorescent microscopy revealed colocalization of nuclear DDX3X and DNA:RNA hybrid foci while the canonical DNA:RNA hybrid regulators, DHX9, DDX1, DDX5, and XRN2 co-immunoprecipitated with DDX3X (Figure 2.6A-C). We used a flow-based assay to measure the retention of dRNaseHI upon DDX3X inhibition which similarly demonstrated decreased DNA:RNA hybrid levels (Supplemental Figure 2.5A; Figure 2.6D). These findings are the first demonstrating a role for DDX3X in regulating global RNA:DNA hybrid levels *in situ*.

We then sought to evaluate this function in the context of DNA damage. Using live cell imaging, we found DNA damage-induced DNA:RNA hybrid levels displayed accumulation kinetics similar to DDX3X-GFP recruitment kinetics (Supplemental Figure 2.5D-E). While *DDX3X* knockdown is not tolerated in the DIvA cell line, we utilized the DDX3X-specific inhibitor, RK-33, to disrupt DDX3X catalytic activity (79). DDX3X inhibition also diminished DNA:RNA hybrid accumulation in live cells upon microirradiation (Figure 2.6E). Using qPCR to specifically detect DNA:RNA hybrids immunoprecipitated with the anti-DNA:RNA hybrid antibody (S9.6), inhibiting DDX3X activity reduced DNA:RNA hybrid formation at the *RBMXL1 AsiSI* site (DSB+) as well as in *RPL13A* (DSB-) upon tamoxifen treatment (Figure 2.6F-G). Intriguingly, RNase I_f-resistant RNA at the *RBMXL1 AsiSI* site was detected upon DDX3X inhibition, suggesting the presence of dsRNA upon DDX3X inhibition (Figure 2.6H).

DDX3X is enriched at DSB sites in the DIvA model

We utilized the novel Cut&Run sequencing method (90) to interrogate DDX3X localization in the genome of the DIvA cell line. DIvA cells were treated with tamoxifen as previously described to induce AsiSI localization to the nucleus for DSB induction, then incubated with anti-DDX3X, anti-Senataxin, or anti-RNA polymerase II. Reads from anti-DDX3X treated samples were enriched at *AsiSI* sites throughout the genome upon tamoxifen treatment relative to untreated controls (Figure 2.7). Interestingly, DDX3X enrichment peaked at the 3’ end of the cut site, while DDX3X was depleted at the 5’ end at precisely the region with the most RNA polymerase II occupancy upon tamoxifen treatment (Figure 2.7A). It is interesting to note the RNA polymerase II is recruited on both sides of the *AsiSI* breaks, consistent with the notion that DSBs induce bi-directional transcription (92). Furthermore, we confirmed the presence of DNA:RNA hybrids at the *AsiSI* sites via the anti-Senataxin antibody (Figure 2.7B). The mutually exclusive enrichment pattern of DDX3X and Senataxin suggests these proteins operate in a stepwise manner related to RNA metabolism.

DSB Repair is sensitive to DDX3X manipulation

Numerous studies suggest that DDX3X affects DNA DSB repair. We aimed to measure DDX3X-dependent DSB repair efficiency comprehensively. In order to assess DDX3X dependent repair in both in both major repair pathways - end-joining (EJ) and homology-directed repair (HDR) - we employed a variety of DDX3X-targeted interventions in a fluorescent reporter system, the traffic light reporter (TLR), stably integrated into HEK293T (Figure 2.8A; Supplemental Figure 2.6A-B). Small molecule inhibition, siRNA mediated knockdown, and putative CRISPR knockout all reduced DSB repair by both EJ and HDR (Figure 2.8B; Supplemental Figure 2.8).

EJ repair activity is thought to be a product of both cNEHJ and alternative end joining (aEJ). Knockdown of Ku70 (*XRCC6*) reduced EJ deficiency upon DDX3X inhibition or knockdown, suggesting DDX3X plays a role in cNHEJ (Figure 2.8C-D). Unfortunately, we were unable to determine the PARP1-dependent pathway DDX3X is involved in due to a synthetic lethal genetic relationship. We recapitulated DDX3X-dependent repair in both repair pathways using the endonuclease AniI as well as measuring EJ repair of linearized pEGFP, suggesting the effect is not a Cas9 artifact (Supplemental Figure 2.6 C-D). Interestingly, ectopic overexpression of DDX3X produces a dominant negative effect which reduces EJ and HDR in a dose-dependent manner (Supplemental Figure 2.7A). This effect was not observed in cells expressing the helicase-deficient mutant (SAT → AAA), but was present with stress granule-deficient (L43A) (Supplemental Figure 2.7B). Collectively, these findings suggest that DDX3X regulates both canonical DSB repair pathways.

Discussion

Consistent with other RNA-related proteins involved with DNA repair processes, our findings highlight that the role of DDX3X in DNA repair is multifactorial. The canonical role of DDX3X as a regulator of gene expression likely influences DNA repair capacity. Indeed, DDX3X-mediated dysregulation of repair factor levels has been suggested to promote liver carcinogenesis (93). Interestingly, our characterization of differentially expressed DNA repair factors upon DDX3X knockdown yielded a paucity of repair protein levels significantly (> 20%) reduced (Figure 2.1). However, the magnitude of protein level changes may also become more pronounced over time. As siRNA knockdown is transient, a stable cell model harboring a heterozygous, hypomorphic *DDX3X* mutation might be used to more accurately define the magnitude of DNA repair protein level changes. Regardless, the DDX3X knockdown reported herein reflected the levels of functional DDX3X seen in cellular disease states. We propose that dysregulation DDX3X-mediated DNA repair protein expression likely does not completely ablate a particular arm of DDR. Rather, an aggregation of DDR protein deficiencies may give rise to genomic instability over time.

Beyond the classical role of RNA-related proteins in gene expression, we found DDX3X plays a direct role in DNA repair. DDX3X colocalization patterns and nuclear interactions highly suggest DDX3X plays a role in DNA repair *in vitro* (Figure 2.2) which is further corroborated by *in vivo* recruitment of DDX3X in a PARP1-dependent manner (Figure 2.3). Accordingly, the importance of the intrinsically disordered domains of DDX3X for recruitment points to a mechanism whereby PARP1 induces recruitment of a subset of RNA-related proteins through liquid-liquid phase separation - akin to the role of DDX3X in cytoplasmic stress granule formation (94; Figure 2.4). This body of research is supported by several mass spectrometry studies identifying DDX3X associated with DNA lesions and repair structures. (95-97)

While the precise function and dynamics of RNA-binding proteins during DSB repair are unknown, DNA:RNA hybrids appear to be important core structures. As suggested by co-immunoprecipitation studies of R-loop protein complexes, we confirmed that endogenous DDX3X co-immunoprecipitated with DNA:RNA hybrid regulators and colocalizes with DNA:RNA hybrids *in situ* (98; Figure 2.6A-C; Appendix Table 2). DDX3X activity was important for global, damage-, and stress- induced hybrid levels (Figure 2.6D-F). Importantly, DDX3X activity played a transcription dependent role in γH2AX activation - a crucial histone modification that facilitates the recruitment of several repair factors (Figure 2.5D). Importantly, the DSB-responsive RNA-binding protein and DDX3X-interactor, FUS, also promotes γH2AX activation during DSB repair (Figure 2.4A; 99). In the DIvA system, Senataxin functions to remove DNA:RNA hybrids that stimulate γH2AX activation (52). Conversely, DDX3X likely promotes programmed DNA:RNA hybrid formation as with Drosha and RBM14 (60, 71). While many RNA-binding proteins suppress transcription at DSB sites, we failed to find alterations in DSB-induced transcriptional repression in the DIvA system (Figure 2.6H). Instead, DHX9 and DDX1 have recently been proposed to regulate DNA:RNA hybrid formation by generating single stranded RNA substrates via unwinding secondary RNA structures (100, 101). As we found RNase I_f-resistant RNA at the *RBMXL1 AsiSI* site (Figure 2.6G), we favor this hypothesis, but acknowledge the current dearth of tools for reliably detecting short dsRNA species that DDX3X may regulate.

MicroRNAs are another, yet less well understood, DSB-induced class of RNA molecules. ATM activation and subsequent DNA damage response foci formation was found to be dependent on damage-induced miRNA biogenesis (102). As γH2AX activation in the DIvA system is regulated by ATM, DDX3X may similarly promote small RNA biogenesis for DSB-induced γH2AX induction (103). Indeed, γH2AX activation in *Danio rerio* larvae was completely dependent on the microRNA processor, Dicer (102). This suggests an interesting line of future investigation for the possible role of DDX3X in DSB-induced microRNA biogenesis.

DSBs are characterized or associated with both PARP1-dependent recruitment of RNA-binding proteins and subsequent RNA metabolism (94). Thus, we aimed to elucidate whether DDX3X supported DSB repair. As suggested in this and prior studies, it is likely that DDX3X affects DSB repair through a combination of regulation of repair protein levels and damage-induced RNA metabolism. It is interesting to note that both under- and over-expression of DDX3X diminished DSB repair in the TLR assay (Supplemental Figure 2.7A). This dosage sensitivity is consistent with X-chromosome gene regulation and recapitulated with RNaseHI dosage sensitivity in similar fluorescent reporter assays (60). The helicase-dependent nature of the overexpression phenotype suggests that RNA metabolism is tightly regulated during DNA repair (Supplemental Figure 2.7B).

The involvement of DDX3X in the major human DSB repair pathway, cNHEJ, has major implications for human health and disease. Clinically, DDX3X has been reported to be both differentially expressed and mutated in numerous cancer types, particularly hematologic malignancies (Ch. 1). Of note, *DDX3X* is most frequently mutated in Burkitt lymphoma, which is characterized by illegitimate break repair resulting in a hallmark translocation between *c-Myc* and the immunoglobulin locus (104). Ddx3x was recently reported to be important for murine lymphocyte development, namely antigen receptor recombination (105, 106). It is, therefore, tempting to speculate that human DDX3X may play an important role in human antigen receptor recombination which is regulated by DNA:RNA hybrid formation and driven by Ku-dependent repair. Finally, similar to other RNA interacting proteins like RNaseH2 (107) and Senataxin (109), germline mutations in this gene are linked to the neurological disorders, *DDX3X* syndrome in females (XX), and generalized intellectual disability in males (XY).

Future Directions

This work creates several exciting lines for the future research of DDX3X. We identify two major areas of interest: the mechanism(s) of DNA repair protein regulation by DDX3X, and the dynamics of DDX3X at DSB sites.

While DDX3X is predominantly known for its role in regulating translation, DDX3X has also been identified as a regulator of transcription. Thus, DDX3X may differentially regulate the expression of the identified DNA repair proteins. For the translation hypothesis, future work will identify binding of DDX3X to DNA repair transcripts, particularly to those predicted to have secondary structures in the 5’ UTR. Techniques such as iCLIP-seq and ribosome profiling can synergistically identify DDX3X-bound transcripts that are translationally regulated. For the transcription hypothesis, parallel ChIP-seq and RNA-seq data can identify genes where DDX3X acts as a co-transcriptional regulator. For both hypotheses, the DDX3X-bound sequences can then be cloned upstream of a reporter gene to confirm their dependence on DDX3X for expression. These approaches will also help to delineate which proteins are dependent on DDX3X for expression, and which protein levels are altered in a compensatory manner.

Future work will also interrogate the precise dynamics of DDX3X associations and localization at DSB sites. Combined with the DIvA cell model, sensitive protein labeling techniques such as APEX can be used to label proteins in the proximity of DDX3X throughout the DSB repair process. Labeled proteins can then be isolated and identified by mass spectrometry. Furthermore, the DDX3X DSB repair interactome could be defined by cell cycle phase, thereby identifying different repair mechanics during NHEJ-prone phases (G_0/G_1) and HDR-prone phases (M/G_2). With regards to the RNA metabolism at sites of breaks, we propose using a modified RNA sequencing approach whereby RNA extracts from DSB induced cells, with impaired DDX3X activity, are first digested to remove single-stranded regions. This would clarify whether DDX3X regulates RNA secondary structure that would otherwise impede the formation of RNA species important for DSB repair.

Chapter 3

Future Directions: Developing CRISPR/Cas9 tools for dissecting the function of *DDX3X* and *DDX3Y* in lymphocyte biology

Sections of this chapter are adapted from a publication and pilot research project.

Xu, Y., Morales, A.J., **Cargill, M.J.**, Towlerton, A.M.H., Coffey, D.G., Warren, E. H., & Tykodi, S.S. Preclinical development of T-cell receptor-engineered T-cell therapy targeting the 5T4 tumor antigen on renal cell carcinoma. *Cancer Immunology, Immunotherapy*. (2019)

Cargill, M.J. and Warren, E.H. Defining the Role of the X-chromosome Gene, *DDX3X*, in Human Lymphopoiesis with CRISPR/Cas9 Technology. Coop Center for Excellence in Hematology. National Institute of Diabetes and Digestive and Kidney Diseases. (2018)

Premise

The studies heretofore have focused on comprehensive characterization of the role of DDX3X in DSB repair. A second line of investigation regards a broader cellular question in a specific cell type - lymphocytes - which rearrange their antigen receptor loci via a process that requires sequence-specific induction and precise repair of DSBs to generate functional antigen receptors (Ch. 1). Classical NHEJ is the DSB repair pathway responsible for generating upwards of a billion unique, circulating antigen receptors (109). The ability of the human immune system to rearrange the T- and B-cell receptor loci with error-free precision is essential for generating the diverse repertoire of antigen receptors necessary to fight infection and cancer. In fact, germline mutations in classical NHEJ genes cause immunodeficiency and somatic aberrances in NHEJ are associated with B- & T- cell malignancies (43). Interestingly, recent studies have also shown a relationship between RNA metabolism and B-cell receptor recombination (101). Thus, lymphocytes are an ideal model for exploring the cellular phenotype of DDX3X-dependent DSB repair.

A number of studies have suggested that both DDX3X and its Y-chromosome homologue, DDX3Y, play important roles in lymphocyte biology. While *DDX3X* is widely expressed, a survey of 27 unique tissue transcriptomes found *DDX3X* and *DDX3Y* transcripts to be most abundant in the bone marrow - the site of lymphocyte development (110). Based on the Human Protein Atlas project, DDX3Y protein was specifically detected in lymphoid-residing tissue such as in tonsil tissue (Figure 3.1; 111). Additionally, *DDX3Y* transcripts were detected in both healthy and malignant immune cells (5). Finally, *DDX3X* is recurrently mutated in a number of blood cancers including chronic lymphocytic leukemia/lymphoma (CLL), NK/T-cell lymphoma, and BL (Ch. 1).

Accordingly, emerging evidence suggests that *DDX3X* plays an important role in lymphocyte development. HSC-specific knockout of *Ddx3x* in male mice leads to a significant reduction in white blood cell levels (105, 106). Lineage-specific analysis by flow cytometry revealed a specific reduction in lymphocyte populations throughout B, T, and NK cell developmental stages, suggesting *Ddx3x* is important for murine lymphopoiesis. Interestingly, total serum IgG levels were elevated, but specific immunoglobulin subtypes were reduced. This points to a role for DDX3X in antigen receptor recombination - the major driver of lymphocyte development. However, the specific effect on antigen receptor recombination and diversification for both BCRs and TCRs remains to be investigated. Furthermore, it is unknown if DDX3X is also important for human lymphopoiesis. We developed CRISPR/Cas9 based technologies for future investigation of the hypotheses that DDX3X and DDX3Y play a role in lymphocyte biology.

Methods

Plasmid construction

Guide RNA sequences (IDT) were cloned into the *BsmBI* restriction site in pLenti-gRNA-RFP (Eleanor Chen lab, University of Washington, Department of Laboratory Medicine and Pathology). The *TRAC* targeted guide RNA (gRNA) sequence was cloned into the pLentiCRISPRv2 vector (Addgene) as specified by the manufacturer’s protocol. DNA fragments encoding a GFP expression cassette flanked by 500 bp homology arms (GeneArt) were cloned into pscAAV (CCEH vector core) between the *BcuI* and *XbaI* restriction sites.

Cell culture and generation

Raji (ATCC) and CD8$^+$ T cells column isolated from donor PBMC samples from healthy adults (Miltenyi Biotec) were cultured in complete RPMI media with 10% FBS or 10% human serum supplemented with beta-mercaptoethanol, respectively. CD8$^+$ T cells were cultured in the presence of 50 U/ mL IL-2 and bead activated with CD3/CD28 Dynabeads® for 48 hrs prior to lentiviral transduction. Human CD34$^+$ HSCs (CCEH) were cultured in serum-free SFEM II supplemented with IL-6, TPO, SCF, Flt3L, SR1, UM171, and Pen/Strep for 36 - 48 hrs prior to electroporation. Human HSCs were electroporated using the P3 Nucleofector kit as specified by the manufacturer using program CY100 with the Nucleofector X (Kiem lab, Fred Hutchinson Cancer Research Center). Raji-Cas9-GFP was generated by lentiviral transduction of Cas9-GFP followed by GFP$^+$ FACS sorting with a BD FACS Aria instrument. Lentiviral particles were generated as described in Chapter 2. Lentiviral particles were harvested after 48 and 72 hrs post-transfection and used to sequentially transduce suspension cells by spinoculation at 32 C, 1200 rpm, for 90 minutes in 8 µg/ mL polybrene for Raji and 5 µg/ mL for T cells, then cultured overnight in the presence of lentivirus. Transduced cells were cultured in fresh media for at least 72 hrs prior to selection or assaying.

Flow cytometry

For measuring viability, cells were stained with Annexin-V (640 nm; Alexa Fluor 700) and DAPI (355 nm; DAPI) as per the manufacturer’s protocol. The viability of target GFP$^+$/RFP$^+$ cells was analyzed on a BD FACS Aria. Transgenic T cells were stained with anti-CD3, anti-CD8, 5T4 tetramer, and DAPI as specified prior to analysis and sorting on a BD FACS Aria.

CellTiter Glo Assay

Cells were seeded in a 96 well plate and treated with the specified drug combinations. Viability was assessed by the CellTiter Glo assay as described by the manufacturer and measured on a Model Centro LB960 microplate luminometer (Immune Monitoring lab).

T7 Endonuclease Assay

Genomic DNA was extracted with a QIAamp Blood Mini kit from CRISPR-edited T cells sorted by CD3 status or Raji cells sorted for Cas9 (GFP) and guide RNA (RFP) expression. The Cas9 target sites were PCR amplified, melted, and reannealed as described by the T7 endonuclease 1 kit manufacturer (NEB). T7 endonuclease was added and digested products were analyzed by gel electrophoresis.

Ch. 3 Reagents Table

Reagent	**Vendor/ Source**	**Working Concentration or Amount (if applicable)**	**Sequence (if applicable)**
pLenti-Cas9-GFP	Chen Lab, UW		
pLenti-gRNA-RFP	Chen Lab, UW		

pLentiCRISPRv2	Addgene		
pscAAV	CCEH		
pTCR-5T4-Clone 17	Warren Lab	1.5 µg	
pRRev	Addgene	1 µg	
pMD2-G	Addgene	0.5 µg	
pRRE	Addgene	1 µg	
BsmBI	Thermo Fisher	30 units/ 5 µg plasmid	
BcuI	Thermo Fisher	30 units/ 5 µg plasmid	
XbaI	Thermo Fisher	30 units/ 5 µg plasmid	
pAAV-SH-GFP	GeneArt		
pAAV-DDX3X-GFP-1	GeneArt		
pAAV-DDX3X-GFP-2	GeneArt		
sgDDX3Y-1	IDT		GCAGTTTAGCGATATTGACA
sgDDX3Y-2	IDT		TCTTGTTGGGGCTAAAACCA
sgTRAC	IDT		GAGAATCAAAATCGGTGAAT
sgSHctrl	IDT		TGAGCACATATTCCACA
T7E1 Kit	NEB		
Effectene	Qiagen	60 µL / rxn	
Lenti-X Concentrator	Clontech	3 mL / 10 mL supernatant	
Human CD8+ T-cell isolation kit	Miltenyi Biotec		
CD3/CD28 Dynabeads® human T-cell expander	Thermo Fisher	1:1 cell:bead ratio	

Polybrene	Sigma-Aldrich	8 µg/ mL	
Annexin Staining Kit	Thermo Fisher		
Anti-CD3-PE			
Anti-CD8-FITC			
5T4 Tetramer			
DAPI			
QIAamp Blood Mini Kit	Qiagen		
CellTiter Glo Assay	Promega		
Cisplatin	Selleckchem	Indicated	
RK-33	Selleckchem	Indicated	
SFEM II	StemCell Technologies		
IL-6	PeproTech	100 ng/mL	
TPO	PeproTech	100 ng/mL	
SCF	PeproTech	100 ng/mL	
Flt3L	PeproTech	100 ng/mL	
SR1	Cellagen Tech	0.75 µM	
UM171	StemCell Technologies	35 nM	
P3 Nucleofector Kit	Lonza		

Results & Future Directions

Targeting DDX3Y in Burkitt lymphoma cell line, Raji

We first transduced Raji with the Cas9-GFP, followed by transduction of RFP-tagged guide RNA expression vectors to induce knockout of DDX3Y and monitored by flow cytometry

(Figure 3.2A-B). A recent CRISPR screen identified *DDX3Y* as an essential gene in the male Burkitt lymphoma cell line, Raji, due to containing a loss-of-function *DDX3X* mutation. We aimed to recapitulate this finding to validate the CRISPR approach for Raji cells. For two different guide RNAs, *DDX3Y*-targeted Raji cells had an increase in apoptotic cells relative to safe harbor control site targeted cells as measured by Annexin and DAPI staining (Figure 3.2B). While no robust DDX3Y-specific antibody has been generated to measure DDX3Y protein, Cas9 editing was confirmed at the *DDX3Y* target sites by T7 endonuclease assay (data not shown).

As DDX3X plays a role in DNA repair and survival, we exposed *DDX3Y*-targeted cells to gamma irradiation to ask whether DDX3Y might play a similar role. Intriguingly, *DDX3Y*-targeted cells had a two-fold increase in apoptotic cells upon irradiation (Supplemental Figure 3.1A). Furthermore, small molecule inhibition of DDX3Y with RK-33 sensitized Raji to cisplatin- and olaparib-induced cell death (Supplemental Figure 3.1B-C). These results suggest DDX3Y may indeed play an essential role in Burkitt lymphoma viability, particularly recovery from DNA damage, and warrants future research.

Endogenous TCR Knockout in Primary CD8+ T Cells

In order to both support the renal cell carcinoma (RCC) immunotherapy research program in our own lab and to provide preliminary evidence for viable in-house blood cell editing, a similar lentiviral CRISPR approach was used to knockout the endogenous TCR in primary human CD8+ T cells (107). Using the pLentiCRISPR lentiviral system, a *TRAC*-targeted CRISPR construct was transduced into human CD8+ T cells and analyzed by flow cytometry after five and again after seven days. Relative to safe harbor control (SHctrl)-targeted cells, endogenous TCR knockout cells were present in upwards of 18% of the population (Figure 3.3A). Cas9 editing at the *TRAC* locus was confirmed by T7 endonuclease assay (Figure 3.3B).

Knockout efficiency was enhanced to 99% by direct electroporation of Cas9:guide RNA ribonucleocomplexes similarly targeting the *TRAC* locus (Figure 3.3C). TCR knockout and control T cells were subsequently transduced with 5T4-specific TCR constructs in order to compare their efficacy in recognizing and killing cells presenting 5T4 peptide - an RCC-specific antigen (Figure 3.3D). Ablation of the endogenous TCR reduced background killing thereby increasing the specificity of transgenic 5T4-targeted cytotoxic T cells (112). Thus, primary human blood cells were successfully manipulated by CRISPR gene editing for experimental use. We propose co-transfecting template DNA encoding a transgenic TCR sequence flanked with sequences homologous to the endogenous TCR locus. This would allow for the simultaneous knock-in of the transgenic TCR and knockout of the endogenous TCR.

DDX3X **Knockout Model in Human HSCs**

The role of DDX3X in human lymphocyte development, particularly antigen receptor diversification, remains to be investigated. We adopted the above approach to edit *DDX3X* in primary human HSCs (Figure 3.4A). However, the knockout target, *DDX3X*, is intracellular and cannot be tracked by flow cytometry. Thus, we aimed to introduce GFP-encoding template AAV vector during the Cas9 editing process. Flanking the GFP expression cassette with sequences homologous to the target site will promote integration and simultaneously disrupt *DDX3X* and express GFP. Sanger sequencing verified the successful cloning of GFP expression cassettes into a scAAV backbone. Additionally, preliminary electroporation of primary HSCs with GFP mRNA resulted in 99% transfection efficiency, verifying our transfection strategy (Figure 3.4B).

Future research will use CRISPR/Cas9 gene editing technology to knock out *DDX3X* in human HSCs for subsequent repopulation in murine bone marrow. Genetically modified populations can then be extracted and characterized by flow cytometry and DNA/RNA sequencing to answer: does DDX3X affect the level of lymphoid lineage cells? And are there aberrances in their gene expression profiles or antigen receptor sequences? Answers to these questions would have profound implications on the pathogenesis of blood cell malignancies, the health consequences of congenital *DDX3X* mutations, and the DDX3X-dependent effects on human immunity.

Summary of Research

This body of research supports the notion that human RNA helicase, DDX3X, is an integral part of the DNA damage and repair response. We argue that DDX3X plays a multifactorial role in DNA repair, namely DSB repair, with important implications for lymphocyte biology.

First, RNA-binding proteins regulate gene expression. Prior research focused on this hypothesis for the role of DDX3X in DSB repair, yet protein-level evidence was lacking. Our whole proteomic analysis of DNA repair protein levels upon DDX3X knockdown revealed widespread dysregulation of repair factors among all canonical repair pathways (Appendix Table 1; Figure 4.1A). Importantly, deficiencies in repair pathways for common lesions (e.g. oxidations, adducts, and nicks) can cause their conversion to DSBs, thereby making DSB repair a core process in maintaining the genome. However, the precise mechanisms of repair protein regulation and the pathological effects remain to be investigated. We believe DDX3X regulates the expression of these genes.

Second, RNA-binding proteins have an emerging function of directly affecting DNA repair, predominantly DSB repair. Indeed, multiple orthogonal assays suggest that DDX3X actively participates in DSB repair. We described a mechanism whereby PARP1 recruits DDX3X through its intrinsically disordered domains to likely regulate RNA metabolism at DSBs. We propose that DDX3X promotes DNA:RNA hybrid formation necessary for repair such as γH2AX activation, but is dispensable for transcriptional repression (Figure 4.1A). Furthermore, we genetically defined the role of DDX3X in both major DSB repair pathways, the roles in which likely are a combination of direct and indirect effects on repair. Importantly, Ku-dependent repair is necessary for antigen receptor recombination and we hypothesize that DDX3X might support lymphocyte development (Figure 4.1B).

Third, several lines of evidence suggest that both DDX3X and DDX3Y play an important role in lymphocyte health and disease. We developed CRISPR/Cas9 platforms to interrogate the genetics of immortalized BL cells, primary CD8+ T cells, and primary CD34+ HSCs. DDX3Y was found to be important for BL viability and recovery from genotoxic insults, suggesting targeting DDX3Y may be a therapeutic strategy for BL in males. Moreover, CRISPR-mediated ablation of the endogenous T cell receptor locus in primary T cells provided the proof-of-principle for using CRISPR to model DDX3X-dependent lymphopoiesis.

Overall, this body of work advances our understanding of the diverse roles that RNA helicases have in human biology. This work addressed prior hypotheses regarding the role of DDX3X in regulating the DNA repair proteome, then characterized a novel active role in DSB repair. Finally, this work extended our ability to investigate the role of DDX3X and DDX3Y in lymphocyte biology - a cell type highly dependent on DSB repair.

References

1. Disteche, C.M. and Berletch, J.B. (2015) X-chromosome inactivation and escape. *J Genet*, **94**, 591-599.
2. Lahn, B.T. and Page, D.C. (1997) Functional coherence of the human Y chromosome. *Science*, **278**, 675-680.
3. Lahn, B.T. and Page, D.C. (1999) Four evolutionary strata on the human X chromosome. *Science*, **286**, 964-967.
4. Bellott, D.W., Hughes, J.F., Skaletsky, H., Brown, L.G., Pyntikova, T., Cho, T.J., Koutseva, N., Zaghlul, S., Graves, T., Rock, S. *et al.* (2014) Mammalian Y chromosomes retain widely expressed dosage-sensitive regulators. *Nature*, **508**, 494-499.
5. Rosinski, K.V., Fujii, N., Mito, J.K., Koo, K.K., Xuereb, S.M., Sala-Torra, O., Gibbs, J.S., Radich, J.P., Akatsuka, Y., Van den Eynde, B.J. *et al.* (2008) DDX3Y encodes a class I MHC-restricted H-Y antigen that is expressed in leukemic stem cells. *Blood*, **111**, 4817-4826.
6. Sharma, D., Putnam, A.A. and Jankowsky, E. (2017) Biochemical Differences and Similarities between the DEAD-Box Helicase Orthologs DDX3X and Ded1p. *J Mol Biol*, **429**, 3730-3742.
7. Chen, C.Y., Chan, C.H., Chen, C.M., Tsai, Y.S., Tsai, T.Y., Wu Lee, Y.H. and You, L.R. (2016) Targeted inactivation of murine Ddx3x: essential roles of Ddx3x in placentation and embryogenesis. *Hum Mol Genet*, **25**, 2905-2922.
8. Wang, T., Birsoy, K., Hughes, N.W., Krupczak, K.M., Post, Y., Wei, J.J., Lander, E.S. and Sabatini, D.M. (2015) Identification and characterization of essential genes in the human genome. *Science*, **350**, 1096-1101.

9. Linder, P. and Jankowsky, E. (2011) From unwinding to clamping - the DEAD box RNA helicase family. *Nat Rev Mol Cell Biol*, **12**, 505-516.

10. Jankowsky, E. (2011) RNA helicases at work: binding and rearranging. *Trends Biochem Sci*, **36**, 19-29.

11. Chao, C.H., Chen, C.M., Cheng, P.L., Shih, J.W., Tsou, A.P. and Lee, Y.H. (2006) DDX3, a DEAD box RNA helicase with tumor growth-suppressive property and transcriptional regulation activity of the p21waf1/cip1 promoter, is a candidate tumor suppressor. *Cancer Res*, **66**, 6579-6588.

12. Wu, D.W., Liu, W.S., Wang, J., Chen, C.Y., Cheng, Y.W. and Lee, H. (2011) Reduced p21(WAF1/CIP1) via alteration of p53-DDX3 pathway is associated with poor relapse-free survival in early-stage human papillomavirus-associated lung cancer. *Clin Cancer Res*, **17**, 1895-1905.

13. Lai, M.C., Lee, Y.H. and Tarn, W.Y. (2008) The DEAD-box RNA helicase DDX3 associates with export messenger ribonucleoproteins as well as tip-associated protein and participates in translational control. *Mol Biol Cell*, **19**, 3847-3858.

14. Heaton, S.M., Atkinson, S.C., Sweeney, M.N., Yang, S.N.Y., Jans, D.A. and Borg, N.A. (2019) Exportin-1-Dependent Nuclear Export of DEAD-box Helicase DDX3X is Central to its Role in Antiviral Immunity. *Cells*, **8**.

15. Lai, M.C., Chang, W.C., Shieh, S.Y. and Tarn, W.Y. (2010) DDX3 regulates cell growth through translational control of cyclin E1. *Mol Cell Biol*, **30**, 5444-5453.

16. Lee, C.S., Dias, A.P., Jedrychowski, M., Patel, A.H., Hsu, J.L. and Reed, R. (2008) Human DDX3 functions in translation and interacts with the translation initiation factor eIF3. *Nucleic Acids Res*, **36**, 4708-4718.

17. Shih, J.W., Tsai, T.Y., Chao, C.H. and Wu Lee, Y.H. (2008) Candidate tumor suppressor DDX3 RNA helicase specifically represses cap-dependent translation by acting as an eIF4E inhibitory protein. *Oncogene*, **27**, 700-714.

18. Valentin-Vega, Y.A., Wang, Y.D., Parker, M., Patmore, D.M., Kanagaraj, A., Moore, J., Rusch, M., Finkelstein, D., Ellison, D.W., Gilbertson, R.J. *et al.* (2016) Cancer-associated DDX3X mutations drive stress granule assembly and impair global translation. *Sci Rep*, **6**, 25996.

19. Zhao, L., Mao, Y., Zhao, Y. and He, Y. (2016) DDX3X promotes the biogenesis of a subset of miRNAs and the potential roles they played in cancer development. *Sci Rep*, **6**, 32739.

20. Geissler, R., Golbik, R.P. and Behrens, S.E. (2012) The DEAD-box helicase DDX3 supports the assembly of functional 80S ribosomes. *Nucleic Acids Res*, **40**, 4998-5011.

21. Snijders Blok, L., Madsen, E., Juusola, J., Gilissen, C., Baralle, D., Reijnders, M.R., Venselaar, H., Helsmoortel, C., Cho, M.T., Hoischen, A. *et al.* (2015) Mutations in DDX3X Are a Common Cause of Unexplained Intellectual Disability with Gender-Specific Effects on Wnt Signaling. *Am J Hum Genet*, **97**, 343-352.

22. Lennox, A.L., Hoye, M.L., Jiang, R., Johnson-Kerner, B.L., Suit, L.A., Venkataramanan, S., Sheehan, C.J., Alsina, F.C., Fregeau, B., Aldinger, K.A. *et al.* (2020) Pathogenic DDX3X Mutations Impair RNA Metabolism and Neurogenesis during Fetal Cortical Development. *Neuron*, **106**, 404-420 e408.

23. Epling, L.B., Grace, C.R., Lowe, B.R., Partridge, J.F. and Enemark, E.J. (2015) Cancer-associated mutants of RNA helicase DDX3X are defective in RNA-stimulated ATP hydrolysis. *J Mol Biol*, **427**, 1779-1796.

24. Scala, M., Torella, A., Severino, M., Morana, G., Castello, R., Accogli, A., Verrico, A., Vari, M.S., Cappuccio, G., Pinelli, M. *et al.* (2019) Three de novo DDX3X variants associated with distinctive brain developmental abnormalities and brain tumor in intellectually disabled females. *Eur J Hum Genet*, **27**, 1254-1259.

25. Grande, B.M., Gerhard, D.S., Jiang, A., Griner, N.B., Abramson, J.S., Alexander, T.B., Allen, H., Ayers, L.W., Bethony, J.M., Bhatia, K. *et al.* (2019) Genome-wide discovery of somatic coding and noncoding mutations in pediatric endemic and sporadic Burkitt lymphoma. *Blood*, **133**, 1313-1324.

26. Love, C., Sun, Z., Jima, D., Li, G., Zhang, J., Miles, R., Richards, K.L., Dunphy, C.H., Choi, W.W., Srivastava, G. *et al.* (2012) The genetic landscape of mutations in Burkitt lymphoma. *Nat Genet*, **44**, 1321-1325.

27. Bol, G.M., Xie, M. and Raman, V. (2015) DDX3, a potential target for cancer treatment. *Mol Cancer*, **14**, 188.

28. Ojha, J., Secreto, C.R., Rabe, K.G., Van Dyke, D.L., Kortum, K.M., Slager, S.L., Shanafelt, T.D., Fonseca, R., Kay, N.E. and Braggio, E. (2015) Identification of recurrent truncated DDX3X mutations in chronic lymphocytic leukaemia. *Br J Haematol*, **169**, 445-448.

29. Pugh, T.J., Morozova, O., Attiyeh, E.F., Asgharzadeh, S., Wei, J.S., Auclair, D., Carter, S.L., Cibulskis, K., Hanna, M., Kiezun, A. *et al.* (2013) The genetic landscape of high-risk neuroblastoma. *Nat Genet*, **45**, 279-284.

30. Jiang, L., Gu, Z.H., Yan, Z.X., Zhao, X., Xie, Y.Y., Zhang, Z.G., Pan, C.M., Hu, Y., Cai, C.P., Dong, Y. *et al.* (2015) Exome sequencing identifies somatic mutations of DDX3X in natural killer/T-cell lymphoma. *Nat Genet*, **47**, 1061-1066.

31. Brandimarte, L., La Starza, R., Gianfelici, V., Barba, G., Pierini, V., Di Giacomo, D., Cools, J., Elia, L., Vitale, A., Luciano, L. *et al.* (2014) DDX3X-MLLT10 fusion in adults with NOTCH1 positive T-cell acute lymphoblastic leukemia. *Haematologica*, **99**, 64-66.

32. Stransky, N., Egloff, A.M., Tward, A.D., Kostic, A.D., Cibulskis, K., Sivachenko, A., Kryukov, G.V., Lawrence, M.S., Sougnez, C., McKenna, A. *et al.* (2011) The mutational landscape of head and neck squamous cell carcinoma. *Science*, **333**, 1157-1160.

33. Dunford, A., Weinstock, D.M., Savova, V., Schumacher, S.E., Cleary, J.P., Yoda, A., Sullivan, T.J., Hess, J.M., Gimelbrant, A.A., Beroukhim, R. *et al.* (2017) Tumor-suppressor genes that escape from X-inactivation contribute to cancer sex bias. *Nat Genet*, **49**, 10-16.

34. Xie, M., Vesuna, F., Tantravedi, S., Bol, G.M., Heerma van Voss, M.R., Nugent, K., Malek, R., Gabrielson, K., van Diest, P.J., Tran, P.T. *et al.* (2016) RK-33 Radiosensitizes Prostate Cancer Cells by Blocking the RNA Helicase DDX3. *Cancer Res*, **76**, 6340-6350.

35. Lin, T.C. (2019) DDX3X Multifunctionally Modulates Tumor Progression and Serves as a Prognostic Indicator to Predict Cancer Outcomes. *Int J Mol Sci*, **21**.

36. Cruciat, C.M., Dolde, C., de Groot, R.E., Ohkawara, B., Reinhard, C., Korswagen, H.C. and Niehrs, C. (2013) RNA helicase DDX3 is a regulatory subunit of casein kinase 1 in Wnt-beta-catenin signaling. *Science*, **339**, 1436-1441.

37. Wu, D.W., Lin, P.L., Wang, L., Huang, C.C. and Lee, H. (2017) The YAP1/SIX2 axis is required for DDX3-mediated tumor aggressiveness and cetuximab resistance in KRAS-wild-type colorectal cancer. *Theranostics*, **7**, 1114-1132.

38. Sun, M., Song, L., Zhou, T., Gillespie, G.Y. and Jope, R.S. (2011) The role of DDX3 in regulating Snail. *Biochim Biophys Acta*, **1813**, 438-447.

39. Sun, M., Zhou, T., Jonasch, E. and Jope, R.S. (2013) DDX3 regulates DNA damage-induced apoptosis and p53 stabilization. *Biochim Biophys Acta*, **1833**, 1489-1497.

40. Phung, B., Ciesla, M., Sanna, A., Guzzi, N., Beneventi, G., Cao Thi Ngoc, P., Lauss, M., Cabrita, R., Cordero, E., Bosch, A. *et al.* (2019) The X-Linked DDX3X RNA Helicase Dictates Translation Reprogramming and Metastasis in Melanoma. *Cell Rep*, **27**, 3573-3586 e3577.

41. Botlagunta, M., Vesuna, F., Mironchik, Y., Raman, A., Lisok, A., Winnard, P., Jr., Mukadam, S., Van Diest, P., Chen, J.H., Farabaugh, P. *et al.* (2008) Oncogenic role of DDX3 in breast cancer biogenesis. *Oncogene*, **27**, 3912-3922.

42. Zhao, L., Mao, Y., Zhao, Y. and He, Y. (2016) DDX3X promotes the biogenesis of a subset of miRNAs and the potential roles they played in cancer development. *Sci Rep*, **6**, 32739.

43. Jackson, S.P. and Bartek, J. (2009) The DNA-damage response in human biology and disease. *Nature*, **461**, 1071-1078.

44. Hanawalt, P.C. and Spivak, G. (2008) Transcription-coupled DNA repair: two decades of progress and surprises. *Nat Rev Mol Cell Biol*, **9**, 958-970.

45. Teng, Y., Yadav, T., Duan, M., Tan, J., Xiang, Y., Gao, B., Xu, J., Liang, Z., Liu, Y., Nakajima, S. *et al.* (2018) ROS-induced R loops trigger a transcription-coupled but BRCA1/2-independent homologous recombination pathway through CSB. *Nat Commun*, **9**, 4115.

46. Marnef, A., Cohen, S. and Legube, G. (2017) Transcription-Coupled DNA Double-Strand Break Repair: Active Genes Need Special Care. *J Mol Biol*, **429**, 1277-1288.

47. Scully, R., Panday, A., Elango, R. and Willis, N.A. (2019) DNA double-strand break repair-pathway choice in somatic mammalian cells. *Nat Rev Mol Cell Biol*, **20**, 698-714.

48. Boboila, C., Alt, F.W. and Schwer, B. (2012) Classical and alternative end-joining pathways for repair of lymphocyte-specific and general DNA double-strand breaks. *Adv Immunol*, **116**, 1-49.

49. Raynard, S., Niu, H. and Sung, P. (2008) DNA double-strand break processing: the beginning of the end. *Genes Dev*, **22**, 2903-2907.

50. Ferguson, D.O. and Alt, F.W. (2001) DNA double strand break repair and chromosomal translocation: lessons from animal models. *Oncogene*, **20**, 5572-5579.

51. Ceccaldi, R., Rondinelli, B. and D'Andrea, A.D. (2016) Repair Pathway Choices and Consequences at the Double-Strand Break. *Trends Cell Biol*, **26**, 52-64.

52. Cohen, S., Puget, N., Lin, Y.L., Clouaire, T., Aguirrebengoa, M., Rocher, V., Pasero, P., Canitrot, Y. and Legube, G. (2018) Senataxin resolves RNA:DNA hybrids forming at DNA double-strand breaks to prevent translocations. *Nat Commun*, **9**, 533.

53. Michelini, F., Pitchiaya, S., Vitelli, V., Sharma, S., Gioia, U., Pessina, F., Cabrini, M., Wang, Y., Capozzo, I., Iannelli, F. *et al.* (2017) Damage-induced lncRNAs control the DNA damage response through interaction with DDRNAs at individual double-strand breaks. *Nat Cell Biol*, **19**, 1400-1411.

54. Britton, S., Dernoncourt, E., Delteil, C., Froment, C., Schiltz, O., Salles, B., Frit, P. and Calsou, P. (2014) DNA damage triggers SAF-A and RNA biogenesis factors exclusion from chromatin coupled to R-loops removal. *Nucleic Acids Res*, **42**, 9047-9062.

55. Vitor, A.C., Sridhara, S.C., Sabino, J.C., Afonso, A.I., Grosso, A.R., Martin, R.M. and de Almeida, S.F. (2019) Single-molecule imaging of transcription at damaged chromatin. *Sci Adv*, **5**, eaau1249.

56. Ohle, C., Tesorero, R., Schermann, G., Dobrev, N., Sinning, I. and Fischer, T. (2016) Transient RNA-DNA Hybrids Are Required for Efficient Double-Strand Break Repair. *Cell*, **167**, 1001-1013 e1007.

57. Chakraborty, A., Tapryal, N., Venkova, T., Horikoshi, N., Pandita, R.K., Sarker, A.H., Sarkar, P.S., Pandita, T.K. and Hazra, T.K. (2016) Classical non-homologous end-joining pathway utilizes nascent RNA for error-free double-strand break repair of transcribed genes. *Nat Commun*, **7**, 13049.

58. Pryde, F., Khalili, S., Robertson, K., Selfridge, J., Ritchie, A.M., Melton, D.W., Jullien, D. and Adachi, Y. (2005) 53BP1 exchanges slowly at the sites of DNA damage and appears to require RNA for its association with chromatin. *J Cell Sci*, **118**, 2043-2055.

59. Tang, K.F. and Ren, H. (2012) The role of dicer in DNA damage repair. *Int J Mol Sci*, **13**, 16769-16778.

60. Lu, W.T., Hawley, B.R., Skalka, G.L., Baldock, R.A., Smith, E.M., Bader, A.S., Malewicz, M., Watts, F.Z., Wilczynska, A. and Bushell, M. (2018) Drosha drives the formation of DNA:RNA hybrids around DNA break sites to facilitate DNA repair. *Nat Commun*, **9**, 532.

61. Cohen, S., Puget, N., Lin, Y.L., Clouaire, T., Aguirrebengoa, M., Rocher, V., Pasero, P., Canitrot, Y. and Legube, G. (2018) Senataxin resolves RNA:DNA hybrids forming at DNA double-strand breaks to prevent translocations. *Nat Commun*, **9**, 533.

62. Sakasai, R., Isono, M., Wakasugi, M., Hashimoto, M., Sunatani, Y., Matsui, T., Shibata, A., Matsunaga, T. and Iwabuchi, K. (2017) Aquarius is required for proper CtIP expression and homologous recombination repair. *Sci Rep*, **7**, 13808.

63. Li, L., Monckton, E.A. and Godbout, R. (2008) A role for DEAD box 1 at DNA double-strand breaks. *Mol Cell Biol*, **28**, 6413-6425.

64. Li, L., Germain, D.R., Poon, H.Y., Hildebrandt, M.R., Monckton, E.A., McDonald, D., Hendzel, M.J. and Godbout, R. (2016) DEAD Box 1 Facilitates Removal of RNA and Homologous Recombination at DNA Double-Strand Breaks. *Mol Cell Biol*, **36**, 2794-2810.

65. Awwad, S.W., Abu-Zhayia, E.R., Guttmann-Raviv, N. and Ayoub, N. (2017) NELF-E is recruited to DNA double-strand break sites to promote transcriptional repression and repair. *EMBO Rep*, **18**, 745-764.

66. Krietsch, J., Caron, M.C., Gagne, J.P., Ethier, C., Vignard, J., Vincent, M., Rouleau, M., Hendzel, M.J., Poirier, G.G. and Masson, J.Y. (2012) PARP activation regulates the RNA-binding protein NONO in the DNA damage response to DNA double-strand breaks. *Nucleic Acids Res*, **40**, 10287-10301.

67. Mastrocola, A.S., Kim, S.H., Trinh, A.T., Rodenkirch, L.A. and Tibbetts, R.S. (2013) The RNA-binding protein fused in sarcoma (FUS) functions downstream of poly(ADP-ribose) polymerase (PARP) in response to DNA damage. *J Biol Chem*, **288**, 24731-24741.

68. Chen, J.K., Lin, W.L., Chen, Z. and Liu, H.W. (2018) PARP-1-dependent recruitment of cold-inducible RNA-binding protein promotes double-strand break repair and genome stability. *Proc Natl Acad Sci U S A*, **115**, E1759-E1768.

69. Hong, Z., Jiang, J., Ma, J., Dai, S., Xu, T., Li, H. and Yasui, A. (2013) The role of hnRPUL1 involved in DNA damage response is related to PARP1. *PLoS One*, **8**, e60208.

70. Abu-Zhayia, E.R., Khoury-Haddad, H., Guttmann-Raviv, N., Serruya, R., Jarrous, N. and Ayoub, N. (2017) A role of human RNase P subunits, Rpp29 and Rpp21, in homology directed-repair of double-strand breaks. *Sci Rep*, **7**, 1002.

71. Jang, Y., Elsayed, Z., Eki, R., He, S., Du, K.P., Abbas, T. and Kai, M. (2020) Intrinsically disordered protein RBM14 plays a role in generation of RNA:DNA hybrids at double-strand break sites. *Proc Natl Acad Sci U S A*, **117**, 5329-5338.

72. Prindle, M.J., Fox, E.J. and Loeb, L.A. (2010) The mutator phenotype in cancer: molecular mechanisms and targeting strategies. *Curr Drug Targets*, **11**, 1296-1303.

73. Morrison, S.J. and Scadden, D.T. (2014) The bone marrow niche for haematopoietic stem cells. *Nature*, **505**, 327-334.

74. Zhang, Q., Iida, R., Yokota, T. and Kincade, P.W. (2013) Early events in lymphopoiesis: an update. *Curr Opin Hematol*, **20**, 265-272.

75. Roth, D.B. (2014) V(D)J Recombination: Mechanism, Errors, and Fidelity. *Microbiol Spectr*, **2**.

76. Shlomchik, M.J. (2008) Sites and stages of autoreactive B cell activation and regulation. *Immunity*, **28**, 18-28.

77. Basso, K. and Dalla-Favera, R. (2015) Germinal centres and B cell lymphomagenesis. *Nature Reviews Immunology*, **15**, 172-184.

78. Heerma van Voss, M.R., Brilliant, J.D., Vesuna, F., Bol, G.M., van der Wall, E., van Diest, P.J. and Raman, V. (2017) Combination treatment using DDX3 and PARP

inhibitors induces synthetic lethality in BRCA1-proficient breast cancer. *Med Oncol*, **34**, 33.

79. Bol, G.M., Vesuna, F., Xie, M., Zeng, J., Aziz, K., Gandhi, N., Levine, A., Irving, A., Korz, D., Tantravedi, S. *et al.* (2015) Targeting DDX3 with a small molecule inhibitor for lung cancer therapy. *EMBO Mol Med*, **7**, 648-669.

80. Dutertre, M., Lambert, S., Carreira, A., Amor-Gueret, M. and Vagner, S. (2014) DNA damage: RNA-binding proteins protect from near and far. *Trends Biochem Sci*, **39**, 141-149.

81. Ui, A., Chiba, N. and Yasui, A. (2020) Relationship among DNA double-strand break (DSB), DSB repair, and transcription prevents genome instability and cancer. *Cancer Sci*, **111**, 1443-1451.

82. Allison, D.F. and Wang, G.G. (2019) R-loops: formation, function, and relevance to cell stress. *Cell Stress*, **3**, 38-46.

83. Domingo-Prim, J., Bonath, F. and Visa, N. (2020) RNA at DNA Double-Strand Breaks: The Challenge of Dealing with DNA:RNA Hybrids. *Bioessays*, **42**, e1900225.

84. Bader, A.S., Hawley, B.R., Wilczynska, A. and Bushell, M. (2020) The roles of RNA in DNA double-strand break repair. *Br J Cancer*, **122**, 613-623.

85. Massip, L., Caron, P., Iacovoni, J.S., Trouche, D. and Legube, G. (2010) Deciphering the chromatin landscape induced around DNA double strand breaks. *Cell Cycle*, **9**, 2963-2972.

86. Navarrete-Perea, J., Yu, Q., Gygi, S.P. and Paulo, J.A. (2018) Streamlined Tandem Mass Tag (SL-TMT) Protocol: An Efficient Strategy for Quantitative (Phospho)proteome

Profiling Using Tandem Mass Tag-Synchronous Precursor Selection-MS3. *J Proteome Res*, **17**, 2226-2236.

87. Certo, M.T., Ryu, B.Y., Annis, J.E., Garibov, M., Jarjour, J., Rawlings, D.J. and Scharenberg, A.M. (2011) Tracking genome engineering outcome at individual DNA breakpoints. *Nat Methods*, **8**, 671-676.

88. Bhatia, V., Barroso, S.I., Garcia-Rubio, M.L., Tumini, E., Herrera-Moyano, E. and Aguilera, A. (2014) BRCA2 prevents R-loop accumulation and associates with TREX-2 mRNA export factor PCID2. *Nature*, **511**, 362-365.

89. Wang, P.H., Schulenberg, G., Whitlock, S., Worden, A., Zhou, N., Novak, S. and Chen, W. (2018) RNase If -treated quantitative PCR for dsRNA quantitation of RNAi trait in genetically modified crops. *BMC Biotechnol*, **18**, 3.

90. Janssens, D.H., Wu, S.J., Sarthy, J.F., Meers, M.P., Myers, C.H., Olson, J.M., Ahmad, K., and Henikoff, S. (2018) Automated in situ chromatin profiling efficiently resolves cell types and gene regulatory programs. *Epigenetics & Chromatin*. **11**: 74.

91. Tsekrekou, M., Stratigi, K. and Chatzinikolaou, G. (2017) The Nucleolus: In Genome Maintenance and Repair. *Int J Mol Sci*, **18**.

92. Pessina, F., Giavazzi, F., Yin, Y., Gioia, U., Vitelli, V., Galbiati, A., Barozzi, S., Garre, M., Oldani, A., Flaus, A., Cerbino, R., Parazzoli, D., Rothenberg, E., and d'Adda di Fagagna, F. (2019) Functional transcription promoters at DNA double-strand breaks mediate RNA-driven phase separation of damage-response factors. *Nat Cell Biol* **10**: 1286-1299.

93. Chan, C.H., Chen, C.M., Lee, Y.W. and You, L.R. (2019) DNA Damage, Liver Injury, and Tumorigenesis: Consequences of DDX3X Loss. *Mol Cancer Res*, **17**, 555-566.

94. Kai, M. (2016) Roles of RNA-Binding Proteins in DNA Damage Response. Int. J. Mol. Sci. 2016, 17, 310. *Int J Mol Sci*, **17**.

95. Berthelot, V., Mouta-Cardoso, G., Hegarat, N., Guillonneau, F., Francois, J.C., Giovannangeli, C., Praseuth, D. and Rusconi, F. (2016) The human DNA ends proteome uncovers an unexpected entanglement of functional pathways. *Nucleic Acids Res*, **44**, 4721-4733.

96. Ming, X., Groehler, A.t., Michaelson-Richie, E.D., Villalta, P.W., Campbell, C. and Tretyakova, N.Y. (2017) Mass Spectrometry Based Proteomics Study of Cisplatin-Induced DNA-Protein Cross-Linking in Human Fibrosarcoma (HT1080) Cells. *Chem Res Toxicol*, **30**, 980-995.

97. Ikura, M., Furuya, K., Matsuda, S., Matsuda, R., Shima, H., Adachi, J., Matsuda, T., Shiraki, T. and Ikura, T. (2015) Acetylation of Histone H2AX at Lys 5 by the TIP60 Histone Acetyltransferase Complex Is Essential for the Dynamic Binding of NBS1 to Damaged Chromatin. *Mol Cell Biol*, **35**, 4147-4157.

98. Cristini, A., Groh, M., Kristiansen, M.S. and Gromak, N. (2018) RNA/DNA Hybrid Interactome Identifies DXH9 as a Molecular Player in Transcriptional Termination and R-Loop-Associated DNA Damage. *Cell Rep*, **23**, 1891-1905.

99. Wang, W.Y., Pan, L., Su, S.C., Quinn, E.J., Sasaki, M., Jimenez, J.C., Mackenzie, I.R.A., Huang, E.J., and Tsai, L-H. (2013) Interaction of FUS and HDAC1 Regulates DNA Damage Response and Repair in Neurons. *Nat Neurosci.* **10,** 1383–1391.

100. Chakraborty, P., Huang, J.T.J. and Hiom, K. (2018) DHX9 helicase promotes R-loop formation in cells with impaired RNA splicing. *Nat Commun*, **9**, 4346.

101. Ribeiro de Almeida, C., Dhir, S., Dhir, A., Moghaddam, A.E., Sattentau, Q., Meinhart, A. and Proudfoot, N.J. (2018) RNA Helicase DDX1 Converts RNA G-Quadruplex Structures into R-Loops to Promote IgH Class Switch Recombination. *Mol Cell*, **70**, 650-662 e658.

102. Francia, S., Cabrini, M., Matti, V., Oldani, A. and d'Adda di Fagagna, F. (2016) DICER, DROSHA and DNA damage response RNAs are necessary for the secondary recruitment of DNA damage response factors. *J Cell Sci*, **129**, 1468-1476.

103. Caron, P., Choudjaye, J., Clouaire, T., Bugler, B., Daburon, V., Aguirrebengoa, M., Mangeat, T., Iacovoni, J.S., Alvarez-Quilon, A., Cortes-Ledesma, F. *et al.* (2015) Non-redundant Functions of ATM and DNA-PKcs in Response to DNA Double-Strand Breaks. *Cell Rep*, **13**, 1598-1609.

104. Giulino-Roth, L. and Cesarman, E. (2012), *Burkitt's Lymphoma*. Springer Nature, pp. 211-226.

105. Szappanos, D., Tschismarov, R., Perlot, T., Westermayer, S., Fischer, K., Platanitis, E., Kallinger, F., Novatchkova, M., Lassnig, C., Muller, M. *et al.* (2018) The RNA helicase DDX3X is an essential mediator of innate antimicrobial immunity. *PLoS Pathog*, **14**, e1007397.

106. Krishnamurthy, D., Seelamneni, H., Ochayon, D., Harley, J.B., and Waggoner, S.N. (2020) Conditional abrogation of *Ddx3x* reveal its essential role in lymphocyte development and partial compensation by Y chromosome. *J Immunol*. **223.** 19

107. Coffin, S.R., Hollis, T. and Perrino, F.W. (2011) Functional consequences of the RNase H2A subunit mutations that cause Aicardi-Goutieres syndrome. *J Biol Chem*, **286**, 16984-16991.

108. Bennett, C.L. and La Spada, A.R. (2015) Unwinding the role of senataxin in neurodegeneration. *Discov Med*, **19**, 127-136.

109. Mora, T., and Walczak, A.M. (2019) How many different clonotypes do immune repertoires contain?. *Current Opinion Syst. Biol.*, **18**, 104-110.

110. Fagerberg, L., Hallstrom, B.M., Oksvold, P., Kampf, C., Djureinovic, D., Odeberg, J., Habuka, M., Tahmasebpoor, S., Danielsson, A., Edlund, K. et al. (2014) Analysis of the human tissue-specific expression by genome-wide integration of transcriptomics and antibody-based proteomics. *Mol Cell Proteomics*, **13**, 397-406.

111. Uhlen, M., Fagerberg, L., Hallstrom, B.M., Lindskog, C., Oksvold, P., Mardinoglu, A., Sivertsson, A., Kampf, C., Sjostedt, E., Asplund, A. et al. (2015) Proteomics. Tissue-based map of the human proteome. *Science*, **347**, 1260419.

112. Xu, Y., Morales, A.J., Cargill, M.J., Towlerton, A.M.H., Coffey, D.G., Warren, E.H. and Tykodi, S.S. (2019) Preclinical development of T-cell receptor-engineered T-cell therapy targeting the 5T4 tumor antigen on renal cell carcinoma. *Cancer Immunol Immunother*, **68**, 1979-1993.

Figure Legends

Figure 2.1 DDX3X regulates DNA repair protein levels in HEK293T cells. (A) DDX3X siRNA-mediated knockdown induces protein level changes in multiple DNA repair pathways (black dots) including classical non-homologous end-joining and homology-directed repair (labeled). Differential protein levels were identified by mass spectrometry relative to siNegative treated cells across two independent experiments performed with technical triplicates with statistical significance, $p < 0.05$ (dotted line). Western blot measuring (B) Rad51 and (C) XRCC6 levels upon DDX3X knockdown which are labeled in (A) with black arrows.

Figure 2.2 DDX3X associates with DNA damage and repair machinery. (A) DNA repair-associated proteins recurrently enriched in anti-DDX3X co-immunoprecipitation fractions are depicted with lines from DDX3X and grouped by function/pathway (Appendix Table 2). Immunofluorescence microscopy reveals colocalization of DDX3X and two candidate DSB repair factors upon gamma irradiation. (B) Representative Z-plane images of non-irradiated (top row) and irradiated (bottom row) HEK293T cells stained with anti-DDX3X and anti-γH2AX or (E) anti-53BP1. Far right panels represent colocalized foci. (C) Representative Z-plane images of a line profile of arbitrary signal intensity (white line, right image) for nuclear DDX3X foci colocalized with γH2AX foci or (F) 53BP1 foci. Intensity was quantified across the line profile (right of the images). (D) Quantification of DDX3X foci colocalized with γH2AX four hours post-irradiation and (G) 53BP1 in non-irradiated and irradiated cells two hours post-irradiation of at least 25 cells across three independent experiments. **** = $p < 0.0001$, unpaired *t*-test with Welch's correction. (H) Representative time-lapse images of the nuclear export deficient mutant DDX3X$_{L19A/L21A}$-GFP (green) and miRFP-Ku70 (red) accumulation. White arrows indicate the site of microirradiation at 20 seconds. (I) Quantification of the average fluorescence intensity at sites of microirradiation, normalized to the accumulation plateau for each fluorescent construct. The black arrow indicates the time of microirradiation at 20 seconds. All quantifications are from three independent experiments.

Figure 2.3 PARP1 regulates recruitment of DDX3X to sites of microirradiation. (A) A schematic of the *PARP1* locus showing the two guide RNA target sites (red triangles) and PCR primers (blue arrows). (B) PCR-based detection of the 70 bp Cas9 deletion at the *PARP1* site in the mixed population (middle lane), *PARP1*-targeted clone (right lane), relative to the parental WT (left lane). (C) Western blot validation of PARP1-deficiency in the *PARP1* KO cell line (right lane) compared to the parental WT line (left lane). (D) Representative images of DDX3X$_{\mathrm{L19A/L21A}}$-GFP and miRFP-Ku70 20 seconds prior to (left column) and 70 seconds post-microirradiation (right column) in parental wild-type HEK293T cells (left) and *PARP1* KO cells (right). (E) Representative images of PARP1 rescue with miRFP-PARP1 (red) co-expressed with DDX3X$_{\mathrm{L19A/L21A}}$-GFP (green) pre- and 70 seconds post-microirradiation in the *PARP1* KO cell line.

Figure 2.4 DDX3X recruitment is mediated by intrinsically disordered domains. (A) RNA-binding proteins that recurrently immunoprecipitated with DDX3X and previously confirmed to be recruited to DSB sites are depicted with lines connected to DDX3X (center; Appendix Table 2). (B) Disorderedness of the interacting RNA-binding proteins from panel A depicted as their Espritz SCORE calculated on PhaSepDB. (C) Schematics of DDX3X$_{\mathrm{L19A/L21A}}$-GFP deletion constructs aligned with the DDX3X Espritz SCORE including the full-length constructs (FL), N-terminal deletion up to amino acid 181 (NTD), C-terminal deletion from amino acid 540 (CTD), and catalytic core-only construct (Cat. Core). (D) Representative images from the live cell imaging assay before (left) and after (right) microirradiation of cells expressing the DDX3X deletion construct series. (E) Quantification of the average proportion of DDX3X construct recruitment events per ten Ku70 foci per experiment across three independent experiments.

Figure 2.5. The role of DDX3X in DNA repair is transcription-dependent. (A) RNA polymerase II subunits that co-immunoprecipitated with DDX3X (Appendix Table 2). (B) Representative images of DDX3X$_{L19A/L21A}$-GFP and miRFP-Ku70 20 seconds pre- (left column) and 70 seconds post- (right column) microirradiation in vehicle treated (left) and actinomycin D treated (right) cells. (C) Quantification of the average fold change in intensity relative to the initial background reading of DDX3XL19A/L21A-GFP in vehicle and actinomycin D-treated samples following microirradiation. (D) Mean immunofluorescent γH2AX signal +/- 95% confidence interval in the DIvA system relative to mock-treated cells per treatment. Cordycepin was used to inhibit transcription. Statistical significance was tested with a student's t-test with Welch's correction from three independent experiments performed in technical quadruplicate. (E) Representative RT-PCR gel image detecting RNA at the *RBMXL1* locus and *RPL13A* locus from DIvA RNA extracts similarly treated as in (D).

Figure 2.6 DDX3X and DNA:RNA hybrid metabolism. (A) Representative immunofluorescence images of nuclei (DAPI, blue) stained for DDX3X (green) and transiently expressing miRFP-dRNaseHI (red) with a colocalization image (white) on the far right. The experiment was repeated with similar results. (B) A representative line profile (white, right image) of nuclear DDX3X (green) and dRNaseHI signal (red) representing DNA:RNA hybrids. (C) DNA:RNA hybrid factors that recurrently co immunoprecipitated with DDX3X, grouped by function (Appendix Table 2). (D) Flow cytometric-based miRFP-dRNaseH relative mean signal normalized to the background upon DDX3X inhibition from two independent experiments. (E) Graph measuring the fold increase in miRFP-RNaseHI at sites of microirradiation (black arrow) as defined by Ku70 over time upon DDX3X inhibition by 10 uM RK-33 pre-treatment for 6 hours from two independent experiments. (F) Fold induction of DRIP-qPCR signal (% input) relative to mock-tamoxifen treated cells in the DIvA system at the *AsiSI*-site in *RBMXL1* and (G) *RPL13A* site. Four independent DRIP experiments were performed. (H) Representative gel image of RNase I_f RT-qPCR assay amplifying *RBMXL1* RNA with and without reverse transcription (RT). The experiment was repeated with similar results.

Figure 2.7. DDX3X is enriched at DSBs in the DIvA model. DSBs were induced in the DIvA cell model, then subjected to Cut&Run sequencing targeting DDX3X, Senataxin, and RNA polymerase II. Line profiles represent the read count per million reads maps of DSB-induced cells (cut) over non-treated cells (uncut), averaged across all AsiSI restricted sites. The fold change in DDX3X-associated reads (blue) is plotted along with RNA polymerase II-associated reads (green; A) and Senataxin-associated reads (orange; B). Fold-change was found to be statistically significant across the plot as determined by the log likelihood ratio test.

Figure 2.8 DDX3X regulates both major DSB repair pathways. (A) Schematic representation of the Traffic Light DSB reporter system, TLR, that measures DSB repair by end-joining (mCherry) and homology directed repair (GFP). (B) Average relative DSB repair activity in the traffic light reporter assay upon the indicated treatments relative to the respective negative controls. (C) Average relative end joining activity of DDX3X inhibited cells upon siXRCC6 (Ku70) knockdown relative to DMSO vehicle treated samples. (D) Average relative end joining activity from double knockdown samples as indicated. The putative knockout experiment was performed twice independently, and the remaining experiments were performed three times independently.

Supplemental Figure 2.1 Verification of DDX3X nuclear coimmunoprecipitation. (A) Representative Coomassie blue-stained gel from nuclear lysates incubated with the indicated antibodies. (B) Western blot imaging verifying DDX3X co-immunoprecipitation with a known nuclear interactor, HNRNPK. (C) Results of the GO pathway enrichment analysis of the combined coimmunoprecipitation experiments. The listed pathways each reached a statistical significance of < 0.01 with a fisher's exact test. (D) Raw coimmunoprecipitation fold enrichment as a function of statistical significance represented as a volcano plot. Each black dot represents a protein, arrow indicates DDX3X.

Supplemental Figure 2.2 Flow gating scheme for traffic light reporter assay. Singlets were first gated by doublet discrimination by far scatter and side scatter prior to gating BFP$_{+}$ cells. Of the BFP$_{+}$ cells, mCherry$_{+}$ cells were gated in the PE-mCherry channel and GFP$_{+}$ cells were gated in the FITC channel. Fluorescent gate boundaries were previously determined by no transfection and Cas9-BFP only transfection controls.

Supplemental Figure 2.3 DDX3X colocalizes with endogenous DSBs at nucleoli. Representative Z-plane image of DDX3X colocalizing with γH2AX at the nucleolar margin (white arrow) in non-irradiated HEK293T cells.

Supplemental Figure 2.4 DDX3X colocalization with γH2AX is RNase sensitive. Permeabilized cells were incubated with RNase A/T cocktail to digest single stranded RNA or buffer only prior to fixation and subsequent staining. (A) Images represent Z-stack projections. (B) Colocalized foci were quantified as previously described across two independent experiments with statistical significance via the student's t-test with Welch's correction.

Supplemental Figure 2.5 Supplemental data for main figure 2.6. (A) Representative flow plot demonstrating dRNaseHI retention in DAPI+ gated nuclei. (B) Representative immunofluorescence images of nuclei (blue) stained for DDX3X (green) and RNA:DNA hybrids (red; using antibody S9.6) with a colocalization image (white) on the far right. (C) A representative line profile (white, right image) of nuclear DDX3X (green) and S9.6 signal (red) representing RNA:DNA hybrids. (D) Representative images of HEK293T cells transiently expressing DDX3X-L19A/L21A-GFP and miRFP-dRNaseHI that were microirriadiated and imaged every five seconds as quantified in (E).

Supplemental Figure 2.6 Supplemental data for main figure 2.8. (A) Average relative end-joining and (B) HDR activity upon knockdown of Ku70 and Rad51, respectively, with western blot verification below (C) Representative experiment of HEK293T-TLR cells pre-treated with 3 μM RK-33 or DMSO vehicle prior to transfection of I-AniI-BFP and pdonorGFP. (D) Representative experiment of HEK293T-TLR cells cotransfected with 400 ng of BamHI digested or undigested pEGFP pre-treated with RK-33 or DMSO vehicle.

Supplemental Figure 2.7 DSB Repair is sensitive to DDX3X dosage in a helicase-dependent manner. (A) Increasing amounts of DDX3X-HA expression vector was co-transfected in the TLR reporter assay and subsequently blotted with anti-HA (top) and measured (bottom). (B) The previous experiment was repeated with the stress granulate deficient mutant (L43A) and helicase-deficient mutant (S382A/T384A) relative to an empty vector and WT control.

Supplemental Figure 2.8 Western blots from Figure 2.8. (A) Whole protein was harvested from siRNA transfected HEK293T-TLR cells 72 hrs post-transfection and stained for DDX3X (red). (B) Protein was harvested from HEK293T-TLR cells transfected with Cas9-BFP and two DDX3X-targeted guide RNA expression vectors 96 hrs post-transfection with BFP+ cells sorted 24 hrs prior to harvest.

Figure 3.1 DDX3X and DDX3Y protein expression levels in human tissue. Data represents a consensus from immunohistochemical staining of the indicated tissues and their subtypes from the Human Protein Atlas project database.

Figure 3.2 Two-step CRISPR/Cas9 gene editing in Raji cells. (A) Flow plot measuring the target Raji-Cas9-GFP+ population transduced with sgRNA-RFP lentiviral particles. Apoptosis was measured as the percent of DAPI and/or Annexin-V positive cells. (B) Raji cells transduced with guide RNA targeting *DDX3Y* had increased apoptosis in GFP$_{+}$/RFP$_{+}$ gated populations as measured by DAPI and Annexin-V staining.

Figure 3.3 CRISPR/Cas9-mediated gene editing of primary CD8+ T cells. (A) T cells were transduced with LentiCRISPRv2 lentiviral particles targeting the *TRAC* locus, then stained for CD3 and TCR expression. TCR knockouts were defined as CD3-/TCR- double negative. (B) Both double negative and double positive T cells were sorted for the T7E1 assay. (C) Cas9/sgTRAC ribonucleocomplexes were electroporated into primary CD8 T cells, then stained for Pan-TCR expression. (D) Confirmation of transgenic expression of the 5T4-specific TCR after endogenous TCR knockout.

Figure 3.4 Modeling hematopoiesis of *DDX3X* KO HSCs. (A) Schematic for CRISPR/Cas9 directed knockout of *DDX3X* in primary HSCs via AAV-templated integration of GFP. Putative *DDX3X* KO HSCs will be GFP+ sorted for subsequent bone marrow engraftment and repopulation assay. (B) Primary HSCs were electroporated with GFP mRNA and measured by flow cytometry 24 hours later.

Supplemental Figure 3.1 DDX3Y regulates Raji survival and recovery from irradiation. (A) Cas9-GFP+ Raji cells were transduced with the indicated sgRNA-RFP vectors followed for irradiation at 5 Gy, then stained with DAPI and Annexin-V, then measured by flow cytometry. Apoptotic cells were defined as DAPI+ and/or Annexin-V+ after 16 hrs. DDX3 small molecule inhibition (RK-33) sensitizes Raji cells to genotoxic drugs. (B, C) Raji cells were seeded in a 96-well plate and treated as indicated for 48 hrs, then lysed and measured via the CellTiterGlo assay as described. Dox = 1 µM Doxorubucin, 2 µM RK-33, Olap = 1 µM Olaparib.

Figure 4.1 Models related to Summary of Research. (A) Proposed model of DDX3X in DSB repair. DDX3X indirectly affects DSB repair by regulating DSB repair protein levels. DDX3X is also an active participant by regulating RNA metabolism at DSB sites necessary for DSB repair. (B) Speculative model for DDX3X in antigen receptor recombination and lymphocyte development. We hypothesize that DDX3X promotes recombination through its role in DSB repair, an essential process in lymphocyte development.

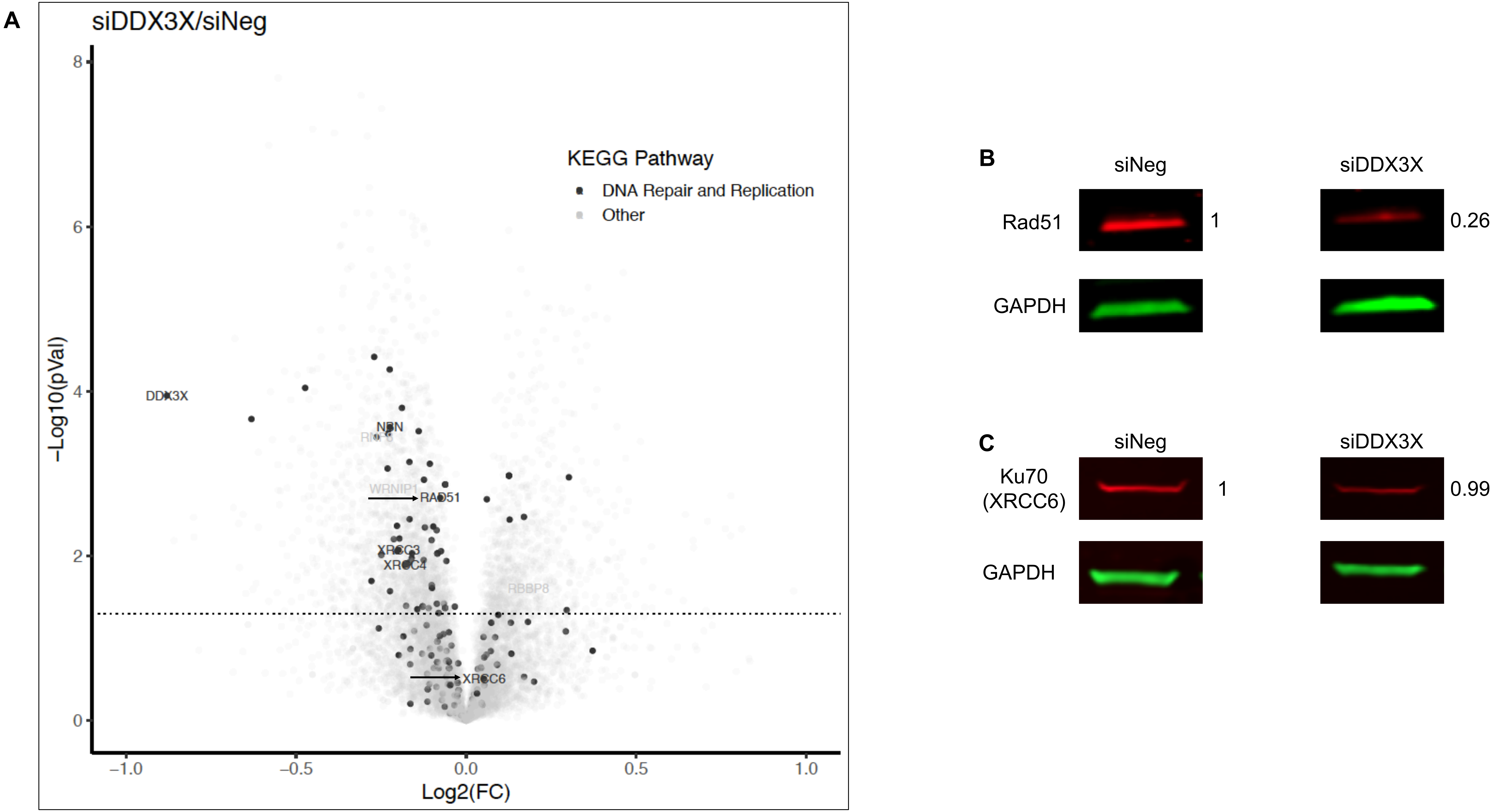
A
siDDX3X/siNeg
KEGG Pathway
● DNA Repair and Replication
● Other
DDX3X
NBN
RNF8
WRNIP1
RAD51
XRCC3
XRCC4
RBBP8
XRCC6
8
6
4
2
0
−Log10(pVal)
−1.0
−0.5
0.0
0.5
1.0
Log2(FC)
B
siNeg
siDDX3X
Rad51
1
0.26
GAPDH
C
siNeg
siDDX3X
Ku70 (XRCC6)
1
0.99
GAPDH

Figure 2.1


A
DNA Recombination
BLM
DNA Repair Recruitment
PARP1
DDX3X
H2AX
Ku70
DNA-PKcs
53BP1
SMC3
DNA Damage Response Histone
NHEJ
Cohesin Complex
B
DAPI
DDX3X
γH2AX
Colocalization
No IR
IR +
C
Intensity
Line Distance
D
Colocalized Foci / Nucleus
****
0
5
10
15
IR -
IR +
E
DAPI
DDX3X
53BP1
Colocalization
No IR
IR +
F
Intensity
Line Distance
G
Colocalized Foci / Nucleus
****
0
5
10
15
20
IR -
IR +
H
0 sec
25 sec
50 sec
75 sec
100 sec
DDX3X^L19A/L21A -GFP
miRFP-Ku70
Merge
I
miRFP-Ku70
DDX3X-GFP
DDX3X-L19A/L21A-GFP
Normalized Intensity
-1.0
-0.5
0.0
0.5
1.0
1.5
2.0
20
40
60
80
100
120
140
Time (sec)

Figure 2.2

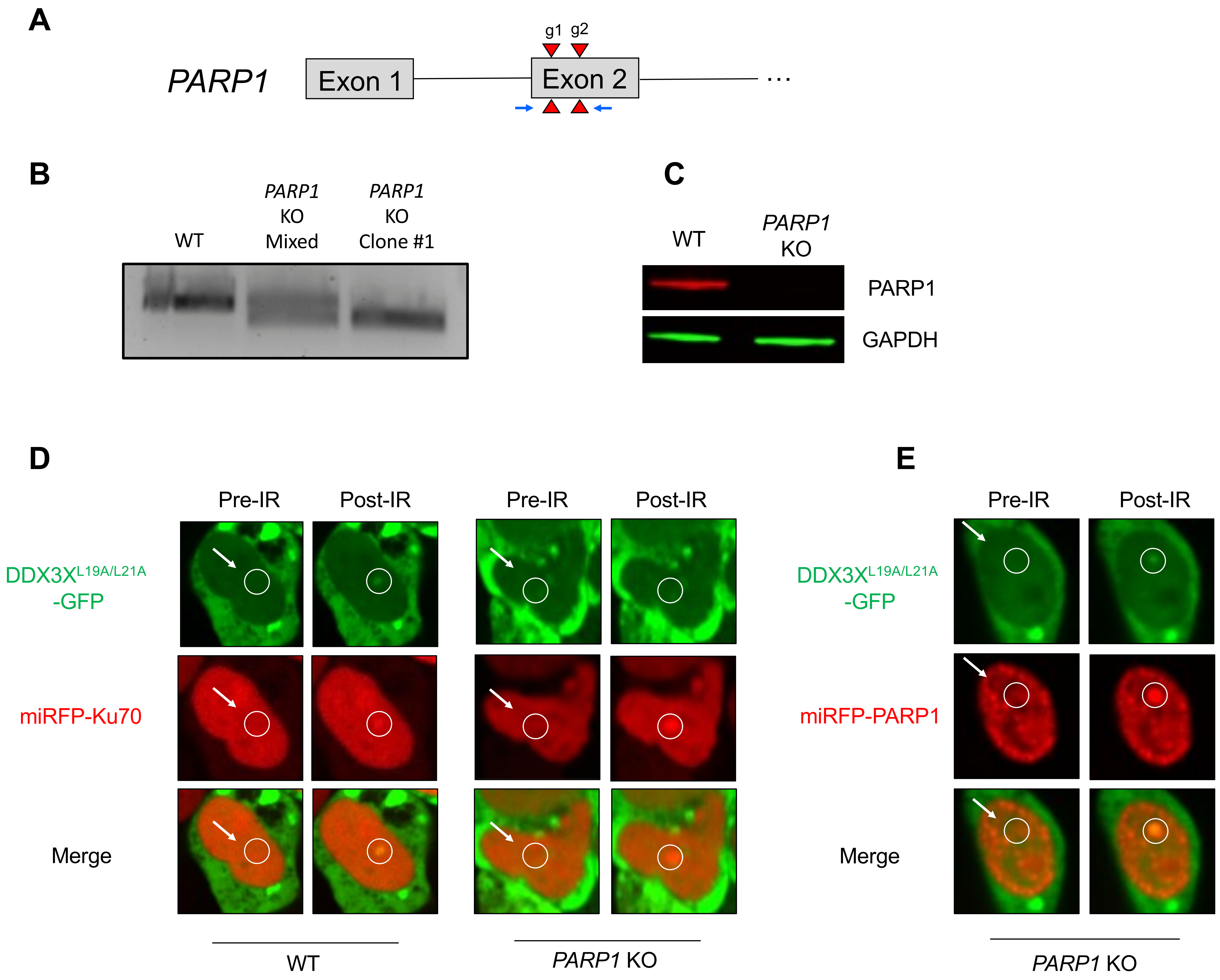
A
PARP1
Exon 1
g1
g2
Exon 2
...
B
WT
PARP1 KO Mixed
PARP1 KO Clone #1
C
WT
PARP1 KO
PARP1
GAPDH
D
Pre-IR
Post-IR
Pre-IR
Post-IR
DDX3X$^{L19A/L21A}$-GFP
miRFP-Ku70
Merge
WT
PARP1 KO
E
Pre-IR
Post-IR
DDX3X$^{L19A/L21A}$-GFP
miRFP-PARP1
Merge
PARP1 KO

Figure 2.3

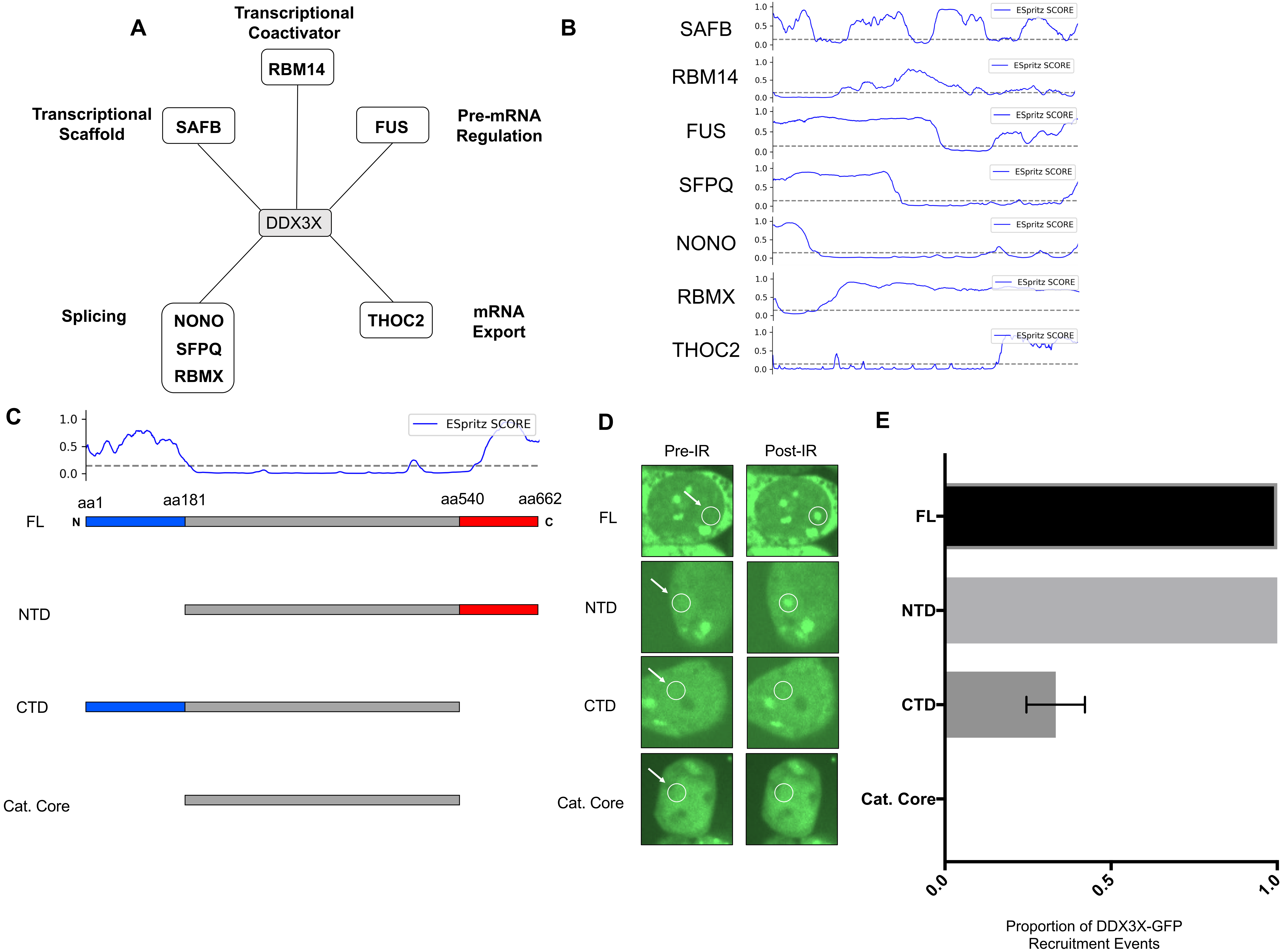
A
Transcriptional Coactivator
RBM14
Transcriptional Scaffold
SAFB
FUS
Pre-mRNA Regulation
DDX3X
Splicing
NONO
SFPQ
RBMX
THOC2
mRNA Export
B
SAFB
RBM14
FUS
SFPQ
NONO
RBMX
THOC2
1.0
0.5
0.0
ESpritz SCORE
C
1.0
0.5
0.0
ESpritz SCORE
aa1
aa181
aa540
aa662
FL
N
C
NTD
CTD
Cat. Core
D
Pre-IR
Post-IR
FL
NTD
CTD
Cat. Core
E
FL
NTD
CTD
Cat. Core
0.0
0.5
1.0
Proportion of DDX3X-GFP Recruitment Events

Figure 2.4


A
DDX3X
RPB1
RPB2
RPB3
RNA Polymerase II
B
Pre-IR
Post-IR
Pre-IR
Post-IR
DDX3X L19A/L21A -GFP
miRFP-Ku70
Merge
Vehicle
Actinomycin D
C
Vehicle
Actinomycin D
Fold Change
1.4
1.2
1.0
0.8
0
20
40
60
80
100
120
140
Time (sec)
D
yH2AX Fold Induction
1.3
1.2
1.1
1.0
0.9
**
ns
DSB: - + - + - + - +
DDX3Xi: - - + + - - + +
Vehicle
Cordycepin
E
DSB -
DSB +
Vehicle
DDX3Xi
Vehicle
DDX3Xi
RBMXL1 AsiSI+
RPL13A AsiSI-

Figure 2.5


A
DAPI
DDX3X
dRNaseHI
Colocalization
B
Intensity
Line Distance
C
DDX3X
DHX9
DDX1
DDX5
DNA/RNA Helicase
XRN2
Exonuclease
D
Relative miRFP-dRNaseHI Intensity
1.2
1.0
0.8
0.6
0.4
0.2
0.0
**
Vehicle
DDX3Xi
E
miRFP-RNaseHI Fold Change
1.20
1.15
1.10
1.05
1.00
0.95
0.90
Vehicle
DDX3Xi
0
20
40
60
80
100
120
Time (sec)
F
RBMXL1
(AsiSI Site +)
OHT
AsiSI
Fold Induction
30
20
10
0
*
OHT:
-
+
-
+
Vehicle
DDX3Xi
G
RPL13A
(Constitutive R Loop +)
OHT
RNA Pol
Fold Induction
2.0
1.5
1.0
0.5
0.0
*
OHT:
-
+
-
+
Vehicle
DDX3Xi
H
RNase I$_f$
-
RNase I$_f$
+
Vehicle
DDX3Xi
Vehicle
DDX3Xi
RT +
RT -

Figure 2.6

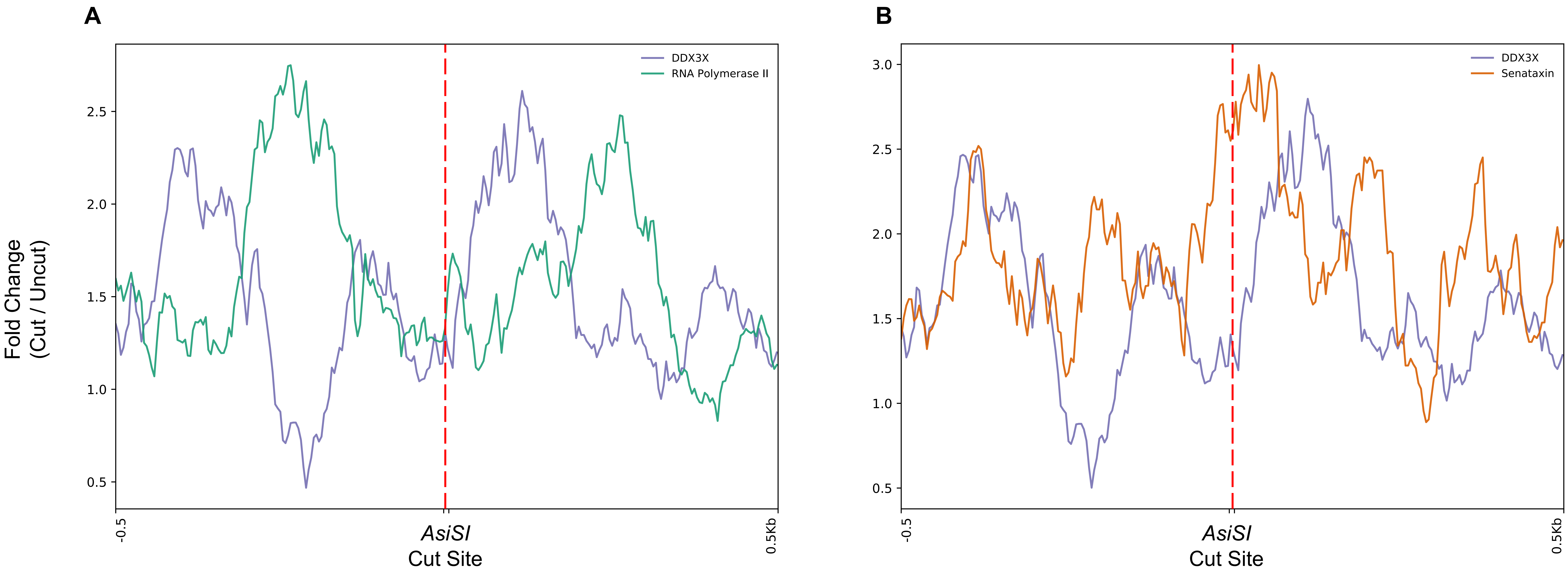
A
B
DDX3X
RNA Polymerase II
DDX3X
Senataxin
Fold Change
(Cut / Uncut)
2.5
2.0
1.5
1.0
0.5
3.0
2.5
2.0
1.5
1.0
0.5
-0.5
AsiSI
Cut Site
0.5Kb
-0.5
AsiSI
Cut Site
0.5Kb

Figure 2.7

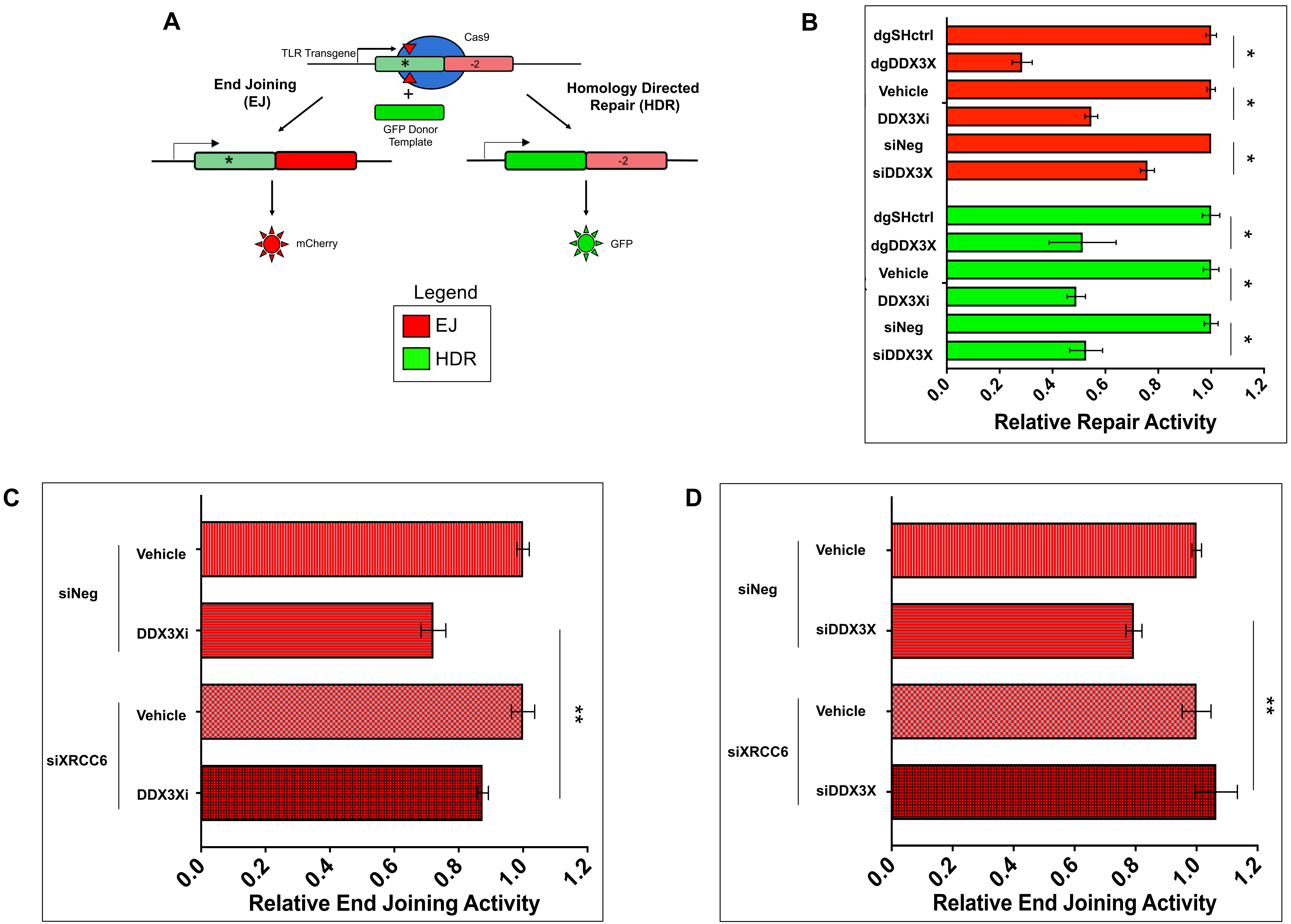
A
TLR Transgene
Cas9
*
-2
+
GFP Donor Template
End Joining (EJ)
Homology Directed Repair (HDR)
*
-2
mCherry
GFP
Legend
EJ
HDR
B
dgSHctrl
dgDDX3X
Vehicle
DDX3Xi
siNeg
siDDX3X
dgSHctrl
dgDDX3X
Vehicle
DDX3Xi
siNeg
siDDX3X
*
*
*
*
*
*
0.0
0.2
0.4
0.6
0.8
1.0
1.2
Relative Repair Activity
C
siNeg
Vehicle
DDX3Xi
siXRCC6
Vehicle
DDX3Xi
**
0.0
0.2
0.4
0.6
0.8
1.0
1.2
Relative End Joining Activity
D
siNeg
Vehicle
siDDX3X
siXRCC6
Vehicle
siDDX3X
**
0.0
0.2
0.4
0.6
0.8
1.0
1.2
Relative End Joining Activity

Figure 2.8

Supplemental Figure 2.1

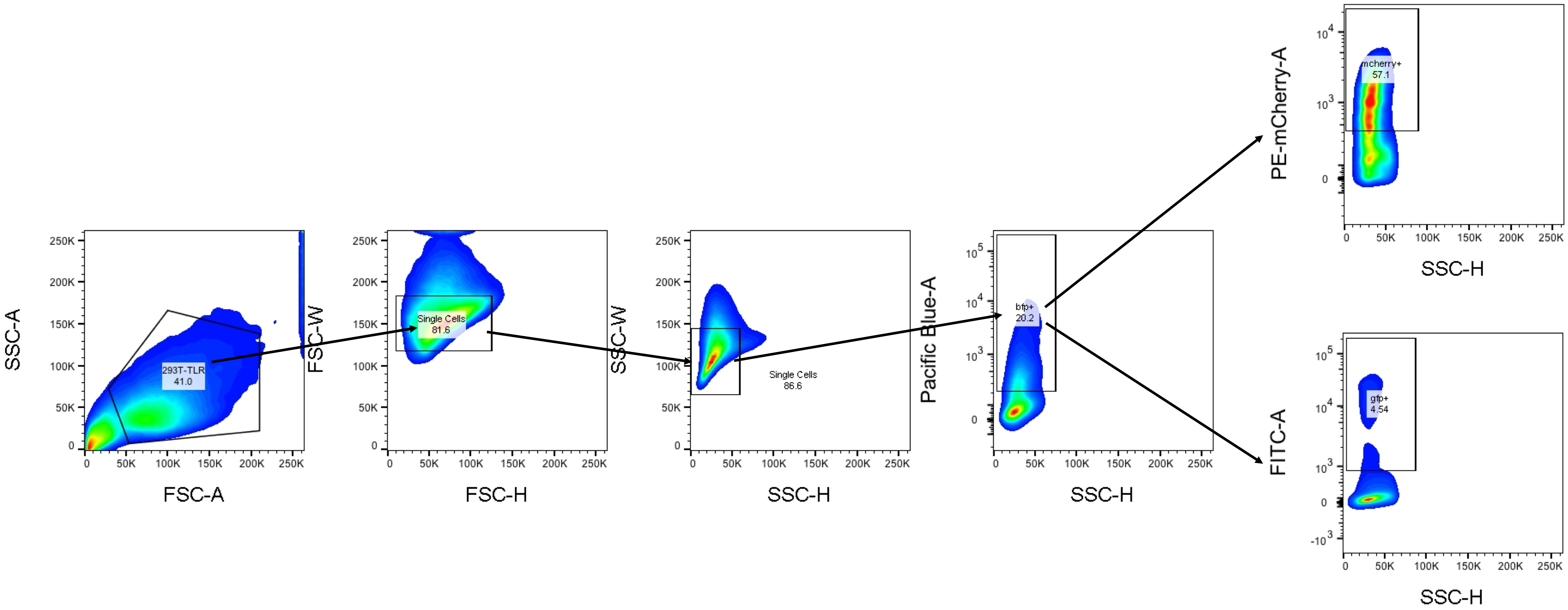

Supplemental Figure 2.2

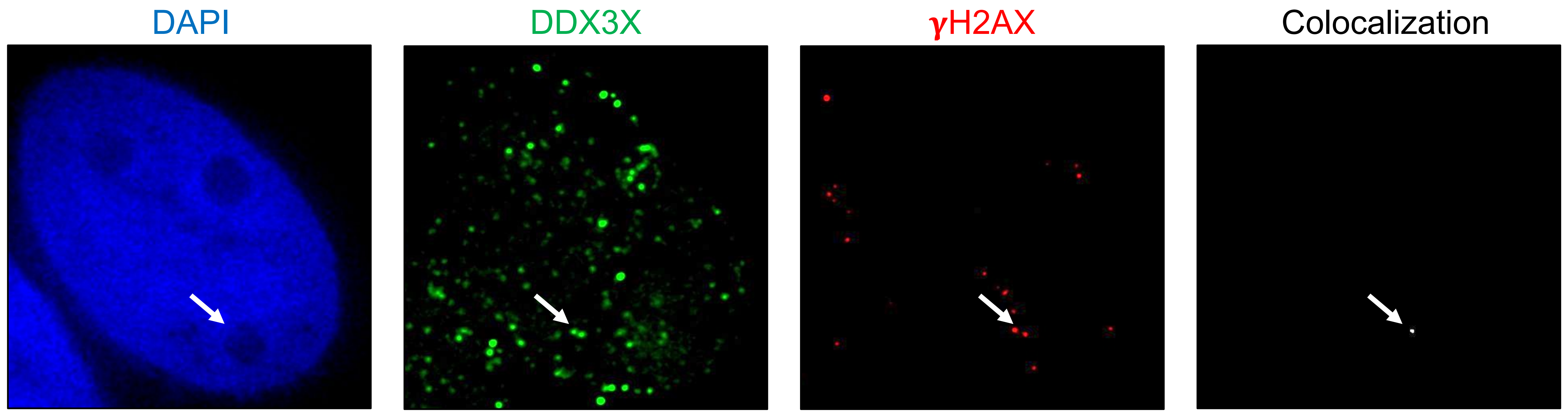

Supplemental Figure 2.3

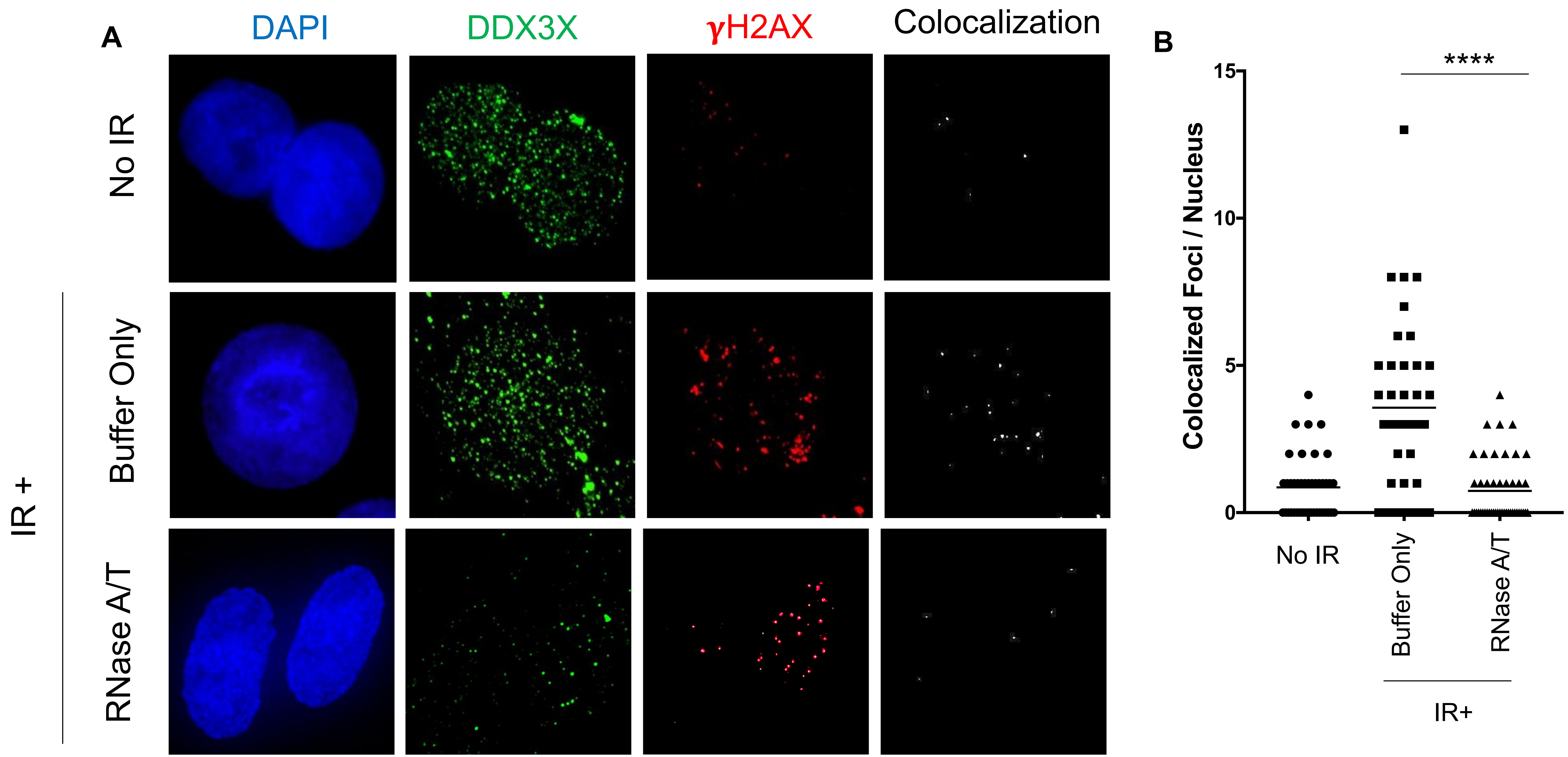

Supplemental Figure 2.4

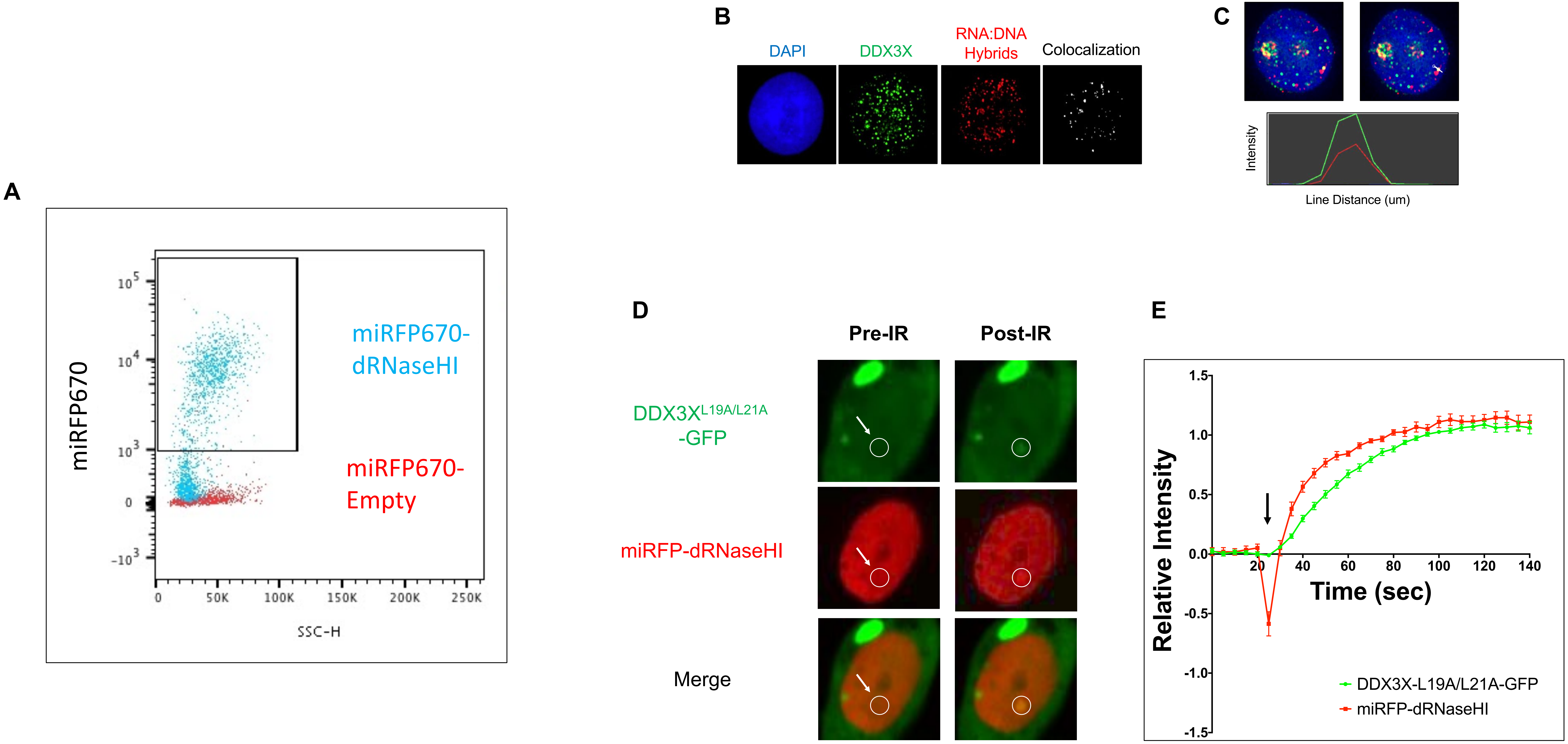

Supplemental Figure 2.5

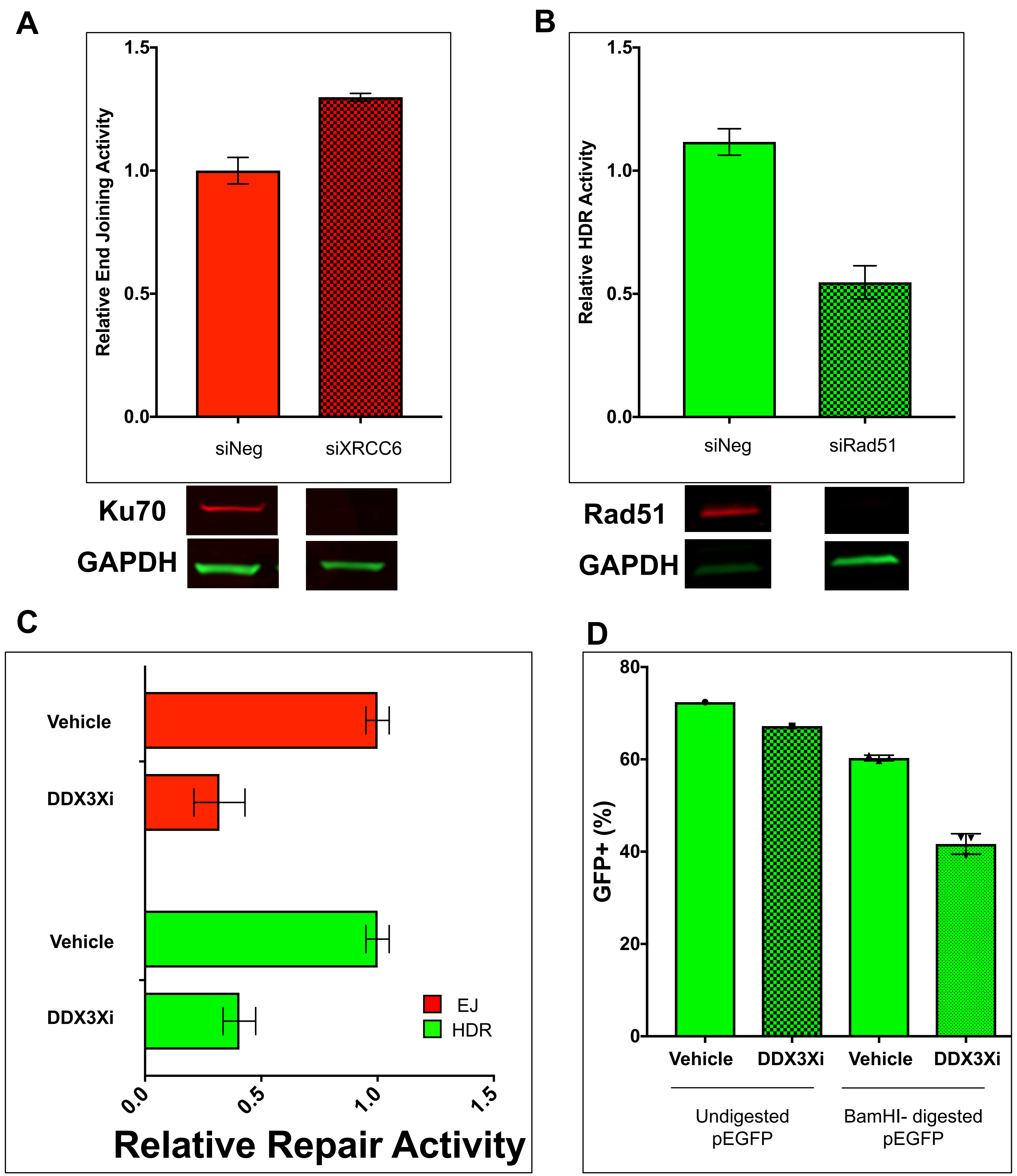

Supplemental Figure 2.6

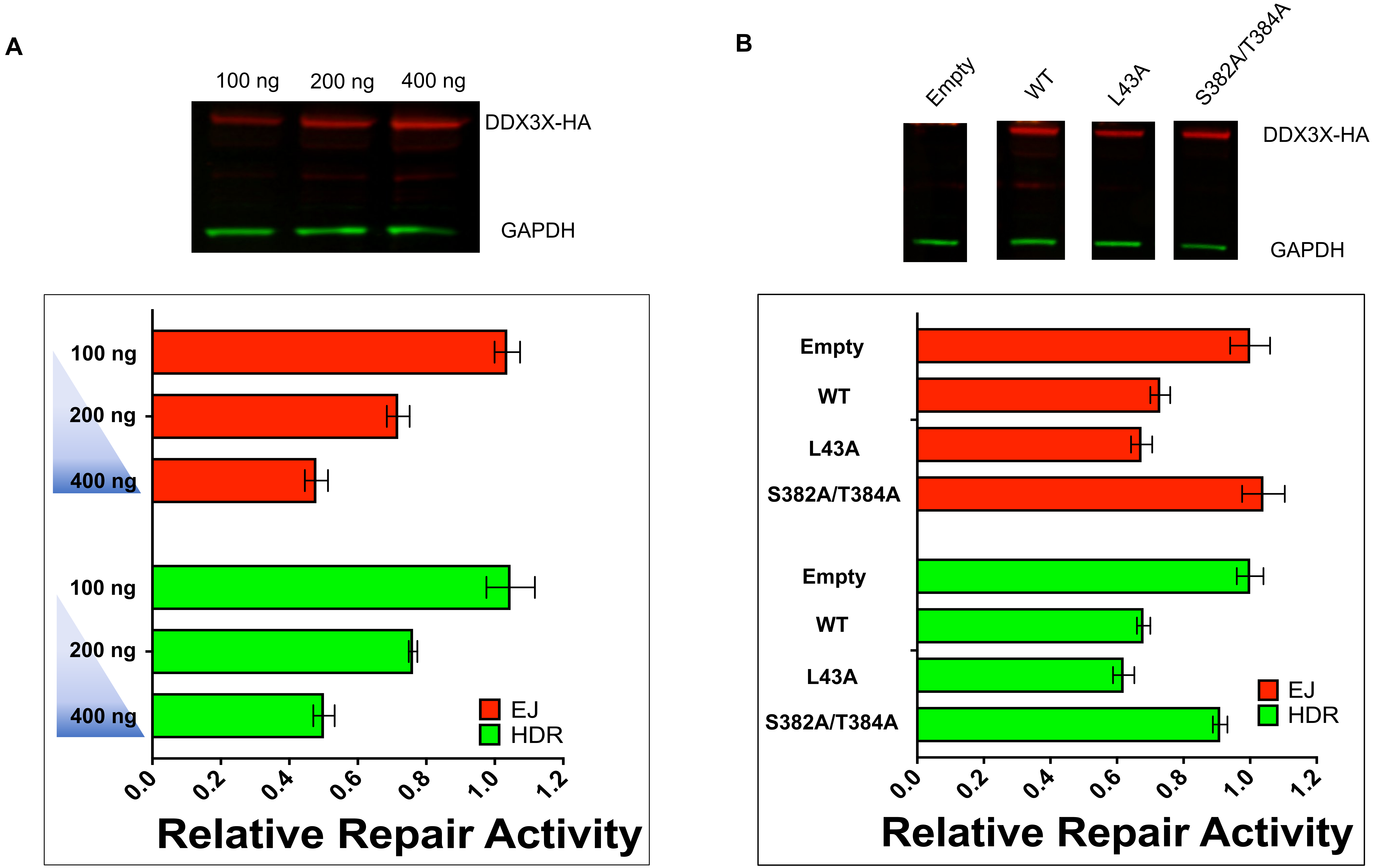

Supplemental Figure 2.7

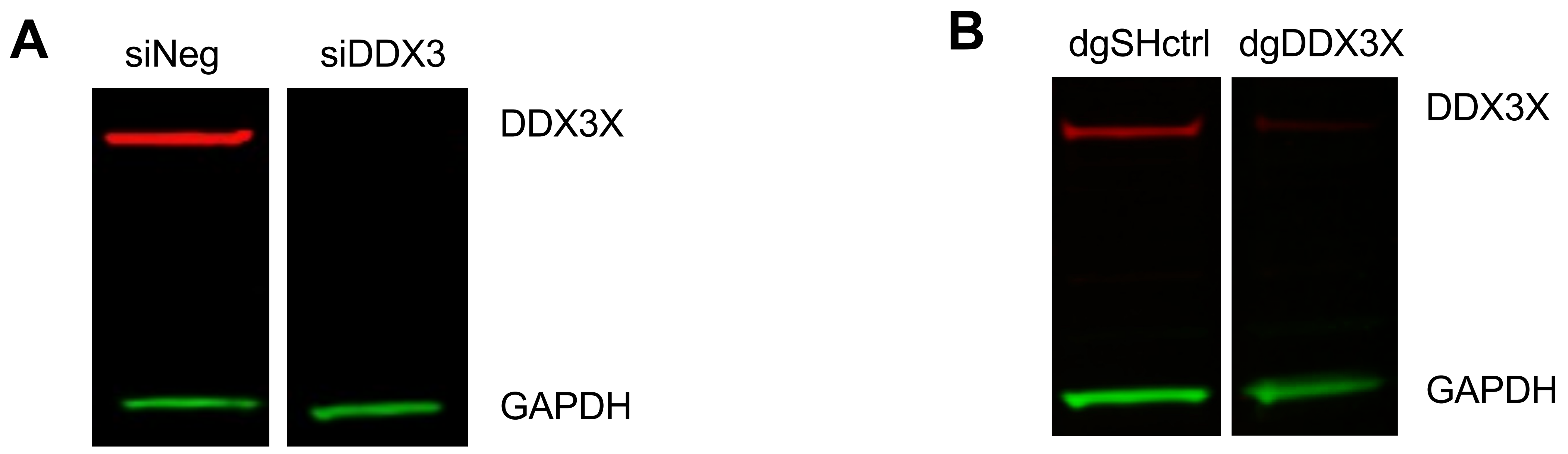

Supplemental Figure 2.8

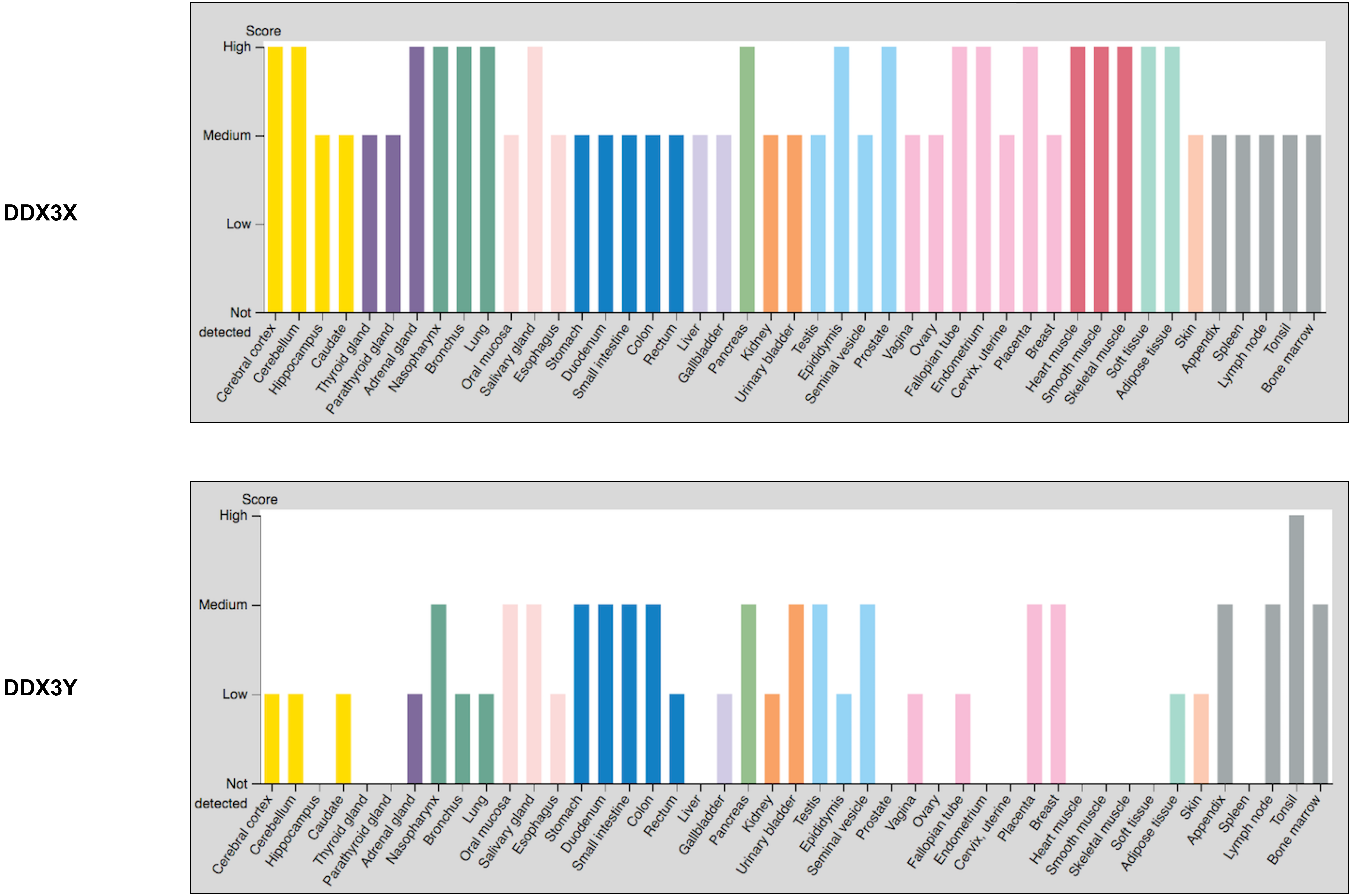
DDX3X
Score
High
Medium
Low
Not detected
Cerebral cortex
Cerebellum
Hippocampus
Caudate
Thyroid gland
Parathyroid gland
Adrenal gland
Nasopharynx
Bronchus
Lung
Oral mucosa
Salivary gland
Esophagus
Stomach
Duodenum
Small intestine
Colon
Rectum
Liver
Gallbladder
Pancreas
Kidney
Urinary bladder
Testis
Epididymis
Seminal vesicle
Prostate
Vagina
Ovary
Fallopian tube
Endometrium
Cervix, uterine
Placenta
Breast
Heart muscle
Smooth muscle
Skeletal muscle
Soft tissue
Adipose tissue
Skin
Appendix
Spleen
Lymph node
Tonsil
Bone marrow
DDX3Y
Score
High
Medium
Low
Not detected
Cerebral cortex
Cerebellum
Hippocampus
Caudate
Thyroid gland
Parathyroid gland
Adrenal gland
Nasopharynx
Bronchus
Lung
Oral mucosa
Salivary gland
Esophagus
Stomach
Duodenum
Small intestine
Colon
Rectum
Liver
Gallbladder
Pancreas
Kidney
Urinary bladder
Testis
Epididymis
Seminal vesicle
Prostate
Vagina
Ovary
Fallopian tube
Endometrium
Cervix, uterine
Placenta
Breast
Heart muscle
Smooth muscle
Skeletal muscle
Soft tissue
Adipose tissue
Skin
Appendix
Spleen
Lymph node
Tonsil
Bone marrow

Figure 3.1

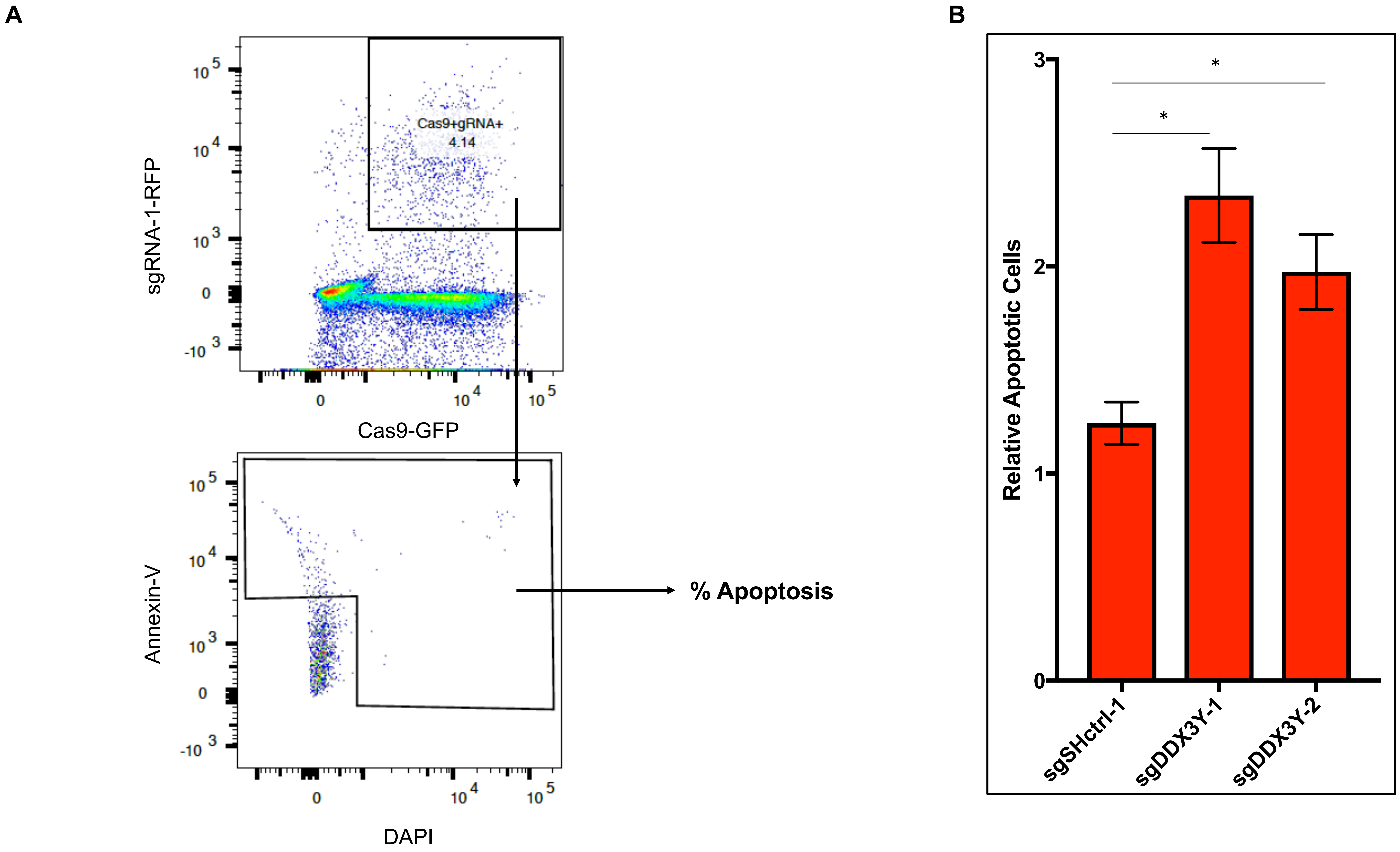
A
sgRNA-1-RFP
10 5
10 4
10 3
0
-10 3
Cas9+gRNA+
4.14
0
10 4
10 5
Cas9-GFP
Annexin-V
10 5
10 4
10 3
0
-10 3
0
10 4
10 5
DAPI
% Apoptosis
B
Relative Apoptotic Cells
3
2
1
0
*
*
sgSHctrl-1
sgDDX3Y-1
sgDDX3Y-2

Figure 3.2


A
Untransduced Control
+LentiCRISPR-sgTRAC (Day 7)
+LentiCRISPR-sgTRAC (Day 10)
Pan-TCR
CD3
Q1 0.10
Q2 98.7
Q4 1.15
Q3 0.090
Q1 0.85
Q2 85.1
Q4 13.7
Q3 0.30
Q1 0.36
Q2 84.3
Q4 15.1
Q3 0.18
B
+LentiCRIPSR-sgTRAC
NTC
CD3+/TCR+
CD3-/TCR-
WT
Cleavage Products
C
Unstained Control
No RNP
+ Cas9/gTRAC RNP
% of max
99.9
Pan-TCR
D
27.2
CD8
5T4p17/HLA-A2

Figure 3.3

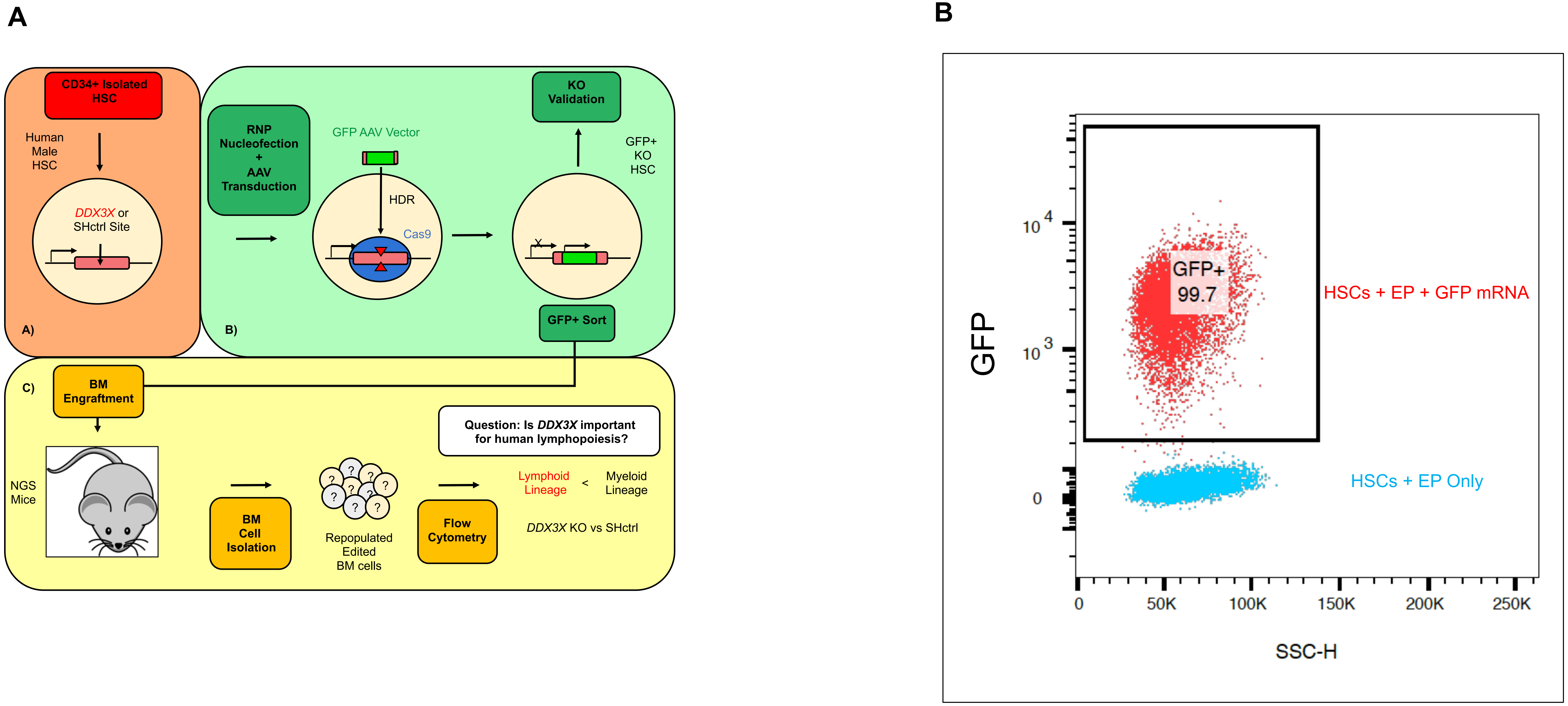
A
CD34+ Isolated HSC
Human Male HSC
DDX3X or SHctrl Site
A)
RNP Nucleofection + AAV Transduction
GFP AAV Vector
HDR
Cas9
KO Validation
GFP+ KO HSC
X
GFP+ Sort
B)
C)
BM Engraftment
NGS Mice
BM Cell Isolation
?
Repopulated Edited BM cells
Flow Cytometry
Question: Is DDX3X important for human lymphopoiesis?
Lymphoid Lineage < Myeloid Lineage
DDX3X KO vs SHctrl
B
GFP
10^4
10^3
0
GFP+ 99.7
HSCs + EP + GFP mRNA
HSCs + EP Only
0
50K
100K
150K
200K
250K
SSC-H

Figure 3.4

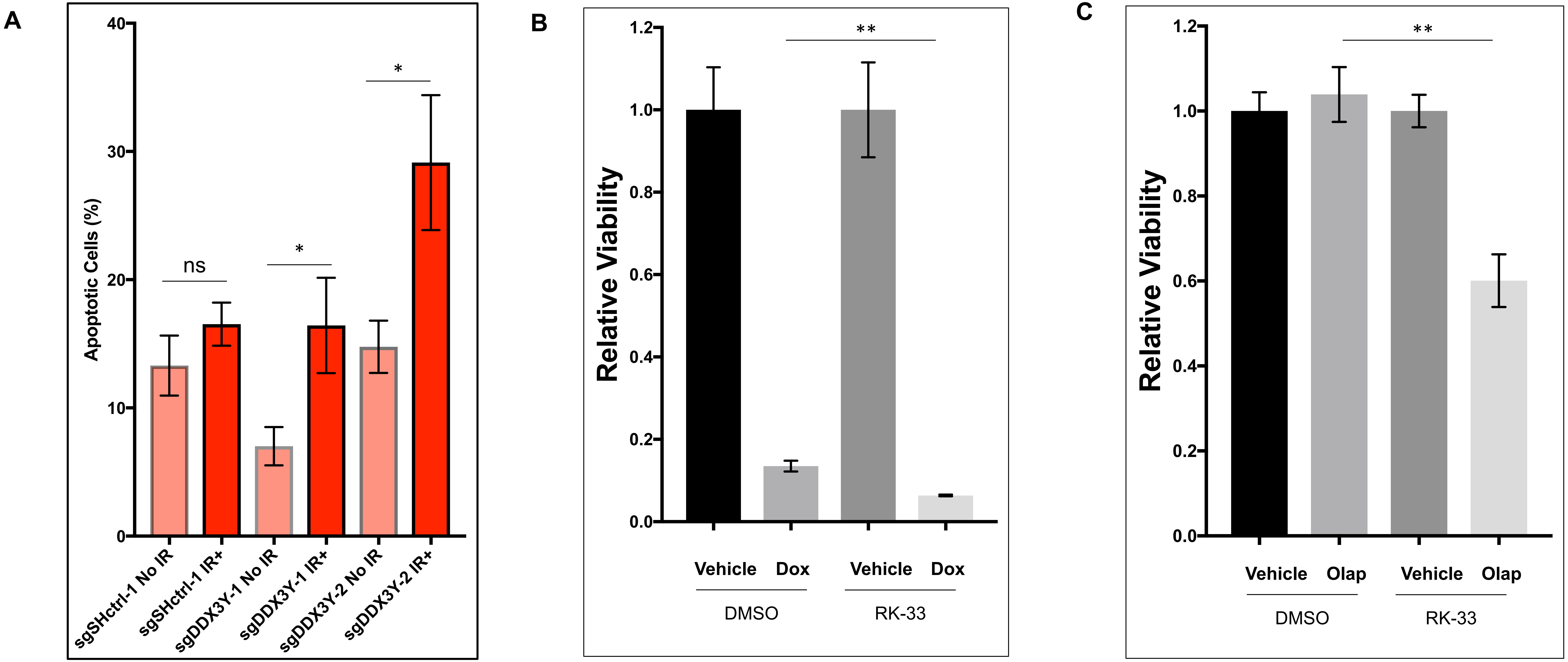

Supplemental Figure 3.1

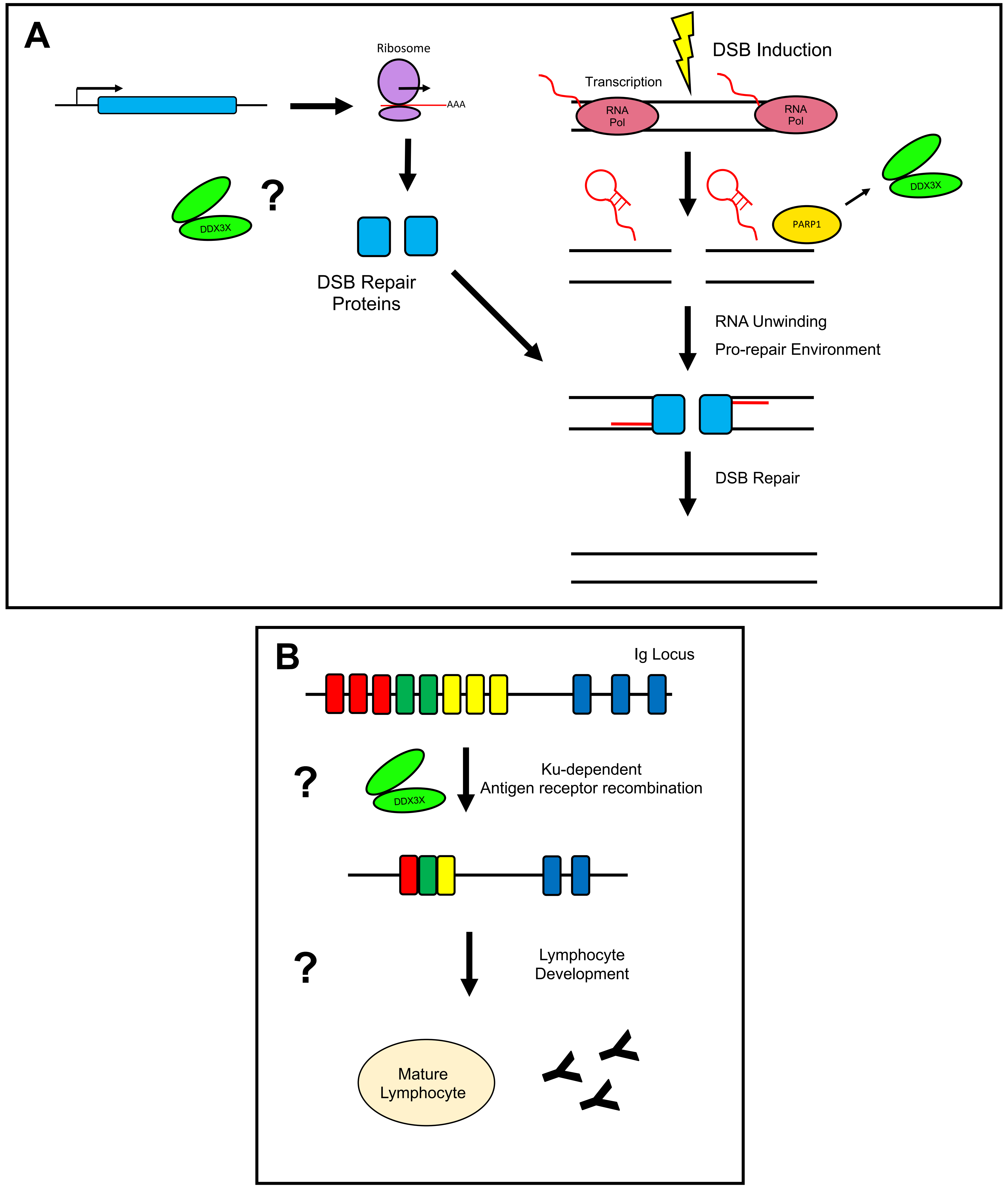
A
Ribosome
AAA
DDX3X
?
DSB Repair
Proteins
DSB Induction
Transcription
RNA
Pol
RNA
Pol
PARP1
DDX3X
RNA Unwinding
Pro-repair Environment
DSB Repair
B
Ig Locus
?
DDX3X
Ku-dependent
Antigen receptor recombination
?
Lymphocyte
Development
Mature
Lymphocyte

Figure 4.1